Turbulent heat flux dynamics along the Dotson and Getz ice-shelf fronts (Amundsen Sea, Antarctica)

Blandine Jacob[1], Bastien Y. Queste[1], and Marcel D. du Plessis[1]

[1]Department of Marine Sciences, University of Gothenburg, Gothenburg, Sweden

Correspondence: Blandine Jacob (blandi.jacob@gmail.com)

Abstract.

In coastal polynyas, where sea–ice formation and melting occur, it is crucial to have accurate estimates of heat fluxes in order to predict future sea–ice dynamics. The Amundsen Sea Polynya is a coastal polynya in Antarctica that remains poorly observed through in situ observations because of its remoteness. Consequently, we rely on models and reanalysis that are unvalidated against observations to study the effect of atmospheric forcing on polynya dynamics. We use austral summer 2022 ship-board data to understand the turbulent heat flux dynamics in the Amundsen Sea Polynya and evaluate our ability to represent these dynamics in ERA5. We show that cold and dry air outbreaks from Antarctica enhance air–sea temperature and humidity gradients, triggering episodic heat loss events. The ocean heat loss is larger along the ice shelf front, and it is also where the ERA5 turbulent heat flux exhibits the largest biases, underestimating the flux by up to 141 W m^{-2} due to its coarse resolution. By reconstructing a turbulent heat flux product from ERA5 variables using a nearest neighbour approach to obtain sea surface temperature, we decrease the bias to 107 W m^{-2}. Using a 1D-model, we show that the mean co-located ERA5 heat loss underestimation of 28 W m^{-2} led to an overestimation of the summer evolution of sea surface temperature (heat content) by +0.76 °C (+8.2×10^7 J) over 35-days. By obtaining the reconstructed flux, the reduced heat loss bias (12 W m^{-2}) reduced the seasonal bias in sea surface temperature (heat content) to -0.17 °C (-3.30×10^7 J) over the 35-days. This study shows that caution should be applied when retrieving ERA5 turbulent flux along the ice shelves, and that a reconstructed flux using ERA5 variables shows better accuracy.

1 Introduction

Among other properties such as momentum, gas and moisture, the atmosphere and the ocean exchange heat, which maintains the Earth's energy balance (Yu, 2019). The climate is highly controlled by the ocean notably because the ocean has the ability to absorb heat from the atmosphere and to redistribute it poleward (Bigg et al., 2003). The ocean is thus the largest heat sink on Earth, absorbing 91 % of the excess heat due to greenhouse gases (Forster et al., 2021). The exchange of heat between the ocean and the atmosphere – or air–sea heat flux – is therefore a crucial process to predict the current and future weather (through heat and moisture released in the atmosphere), upper-ocean physics (sea surface temperature SST variability, sea–ice formation and melting, heat content HC in the mixed-layer), climate (e.g. teleconnection such as el Niño) and the ensuing impacts on society (e.g. agriculture, health, water resource) (Cronin et al., 2019). Because of air–sea heat fluxes' importance,

the scientific community calls for reducing uncertainties to have better flux estimates (Cronin et al., 2019). By increasing the number of observations, our understanding of fluxes can be enhanced and the associated uncertainties reduced (Cronin et al., 2019; Swart et al., 2019; Yu, 2019; Bourassa et al., 2013).

Polar regions are poorly observed because of their remoteness and harsh conditions, which implies we have a particular
30 lack of understanding of the flux dynamics there. In particular, the Southern Ocean south of 60° S has been identified by Swart et al. (2019) as a targeted observation region for the ongoing decade. The Amundsen Sea, West Antarctica (Fig. 1), is a shelf sea south of 60° S seasonally covered by sea–ice and with few historical observations. However, scientific efforts have been concentrated there recently, for example through the International Thwaites Glacier Collaboration (Turner et al., 2017; Scambos et al., 2017), due to adjacent melting glaciers and one of the most biologically productive coastal polynyas (the
35 Amundsen Sea Polynya; ASP) in the Antarctic (Arrigo and van Dijken, 2003).

Polynyas are defined based on their opening mechanism. The ASP is a wind-driven latent heat polynya that forms along the coastline. It has a mean open water area in the austral summer of $27{,}333 \text{ km}^2 \pm 8749 \text{ km}^2$ and an average duration of 131.9 ± 17.5 days over 1997–2010 (Arrigo et al., 2012). In comparison to the surrounding sea–ice that acts as a lid, the polynya operates as an open window that enables direct exchange with the atmosphere (Smith Jr and Barber, 2007). During winter,
40 shelf water latent heat polynyas like the ASP usually inherit the "sea–ice factory" nickname (Morales Maqueda et al., 2004; Ohshima et al., 1998) because sea–ice is continually created and conveyed away by winds or currents. On the other hand, in summer the latent heat polynyas are "ice–melting factories" as the low albedo of open–water compared to surrounding sea–ice favours solar heating, resulting in melting sea–ice. To be able to better predict sea–ice formation and melting in the Amundsen Sea, we therefore need to improve our knowledge of heat exchange in the ASP region.

45 Air–sea heat fluxes must also be considered in the context of the broader atmospheric circulation. In the Southern Ocean near the Polar Front, at 54° S, 89° W, Ogle et al. (2018) show that the advection of cold and dry air triggers ocean heat loss. In the Amundsen Sea, Papritz et al. (2015) showed from ERA-Interim data that the Amundsen Sea is a hotspot for cold air outbreaks (CAOs), which contribute to the turbulent loss. CAOs are equatorward intrusion of cold air over the warmer ocean (Papritz et al., 2015). The large-scale atmospheric system also impacts sea–ice: in 2022 the Amundsen Sea Low (ASL), a quasi
50 stationary low pressure center, has enhanced sea–ice melting (Turner et al., 2022; Yadav et al., 2022).

Without air–sea heat flux observations available, previous studies in the Amundsen Sea or other Antarctic coastal seas have relied on global reanalyses products (e.g., Kumar et al., 2021; Zhou et al., 2022; Yu et al., 2023; Papritz et al., 2015). A global climate reanalysis product combines observations and past forecasts through data assimilation, providing gridded data with a regular temporal resolution. ERA5 reanalysis, produced by the European Centre for Medium–range Weather Forecasts
55 (ECMWF; Hersbach et al., 2020) and its predecessor (ERA–Interim) are considered the most robust reanalyses in Antarctica (Bromwich et al., 2011; Bracegirdle and Marshall, 2012) and in the Amundsen Sea (Jones et al., 2016; Jones, 2018). However, ERA5's ability to reproduce the flux magnitude and variability in the Amundsen Sea, particularly near important boundaries such as ice shelf fronts, has not been validated.

The air–sea heat flux has two components: the radiative flux (sum of the shortwave and longwave radiation) and the turbulent
60 flux (sum of the sensible and latent fluxes). The turbulent heat flux is the main air–sea heat flux component during winter,

2

whereas the radiative component dominates during summer (Morales Maqueda et al., 2004). Despite the importance of the radiative component in summer, key atmospheric conditions could set the scene for important episodic heat loss events. We hypothesize that the Amundsen Sea has a high potential for turbulent loss due to cold dry air and relatively warm SST in summer (above freezing temperature). We perform the first study of turbulent heat flux (THF) in the Amundsen Sea based on austral summer in situ observations and we (i) identify the temporal and spatial variability of the 2022 THF from shipboard observations, (ii) assess ERA5 accuracy at representing these fluxes, and (iii) investigate the relative importance of THF on the summer evolution of SST. Our findings provide evidence of the synoptic-scale air–sea interactions in the ASP and their impact on the summer evolution of SST.

2   Data and methods

2.1   Data

2.1.1   Observations: shipboard and glider data

The meteorology system and thermosalinograph of the Research Vessel (RV) *Nathaniel B. Palmer* recorded variables listed in Table 1 during 57 days. We use these observations to compute the bulk THF; the computation method is described in Sec. 2.2.1. The ship departed Punta Arenas (Chile) on 6 January 2022, reaching the Amundsen Sea (72° S, 117° W) on 15 January 2022. It then entered the polynya region and spent 31 days within 20 km of Dotson or Getz ice shelves, and finally left the polynya region on 25 February 2022 (Fig. 1b). To determine the THF and be consistent with ERA5's temporal resolution, we compute hourly means of the variables in Table 1. The initial resolution was 1-minute. Hourly position of the ship is used to create a classification: Southern Ocean, open ocean in the polynya region (ship more than 20 km away from the coastline), in front of Dotson or Getz ice shelves (ship within 20 km), and in a sea–ice covered region (where the sea–ice concentration; SIC; is larger than 0.15). The RV *Nathaniel B. Palmer* presumably avoided regions of higher sea ice concentration on its transit to the Amundsen Sea. Airflow distortion caused by the superstructure of the RV *Nathaniel B. Palmer* on the wind speed values was negligible (Appendix A, Fig. A1), we therefore did not perform any correction. Several Conductivity Temperature and Depth (CTD) casts were taken during the research campaign. In the present study we use one, taken at 74.02°S, 113°W in front of Dotson Ice Shelf (Fig. 1a, blue square) to initialise the 1D PWP model (see the model description in Sec. 2.2.2).

Variable	Unit	Sensor	Height [m]
Air temperature	°C	R.M. Young 41372LC	19.2
SST	°C	Sea–Bird SBE 38	∼ -6
Wind speed	m s^{-1}	Gill 1390-PK-062	34.4
Relative humidity	%	R.M. Young 41372LC	19.2
Longwave radiation	W m^{-2}	Eppley PIR	33.78
Shortwave radiation	W m^{-2}	Eppley PSP	33.78

Table 1. Sensors installed and variables used in this study recorded by the RV *Nathaniel B. Palmer*.

85   We use Conservative Temperature, Absolute Salinity and pressure from an ocean profiling Seaglider that was deployed during the ship campaign to compute the daily HC in the upper 40 m of the water column. The glider was deployed on 17 January 2022 in front of Dotson ice shelf (73.8° S, 112.6° W). It sampled to the seabed, with a maximum of 901 meters, surfacing between each dive. The glider then headed south towards the ice shelf, and returned north along the Dotson–Getz trough, before being recovered on 4 February 2022 (red transect, Fig. 1a). A total of 286 profiles were collected. The data are

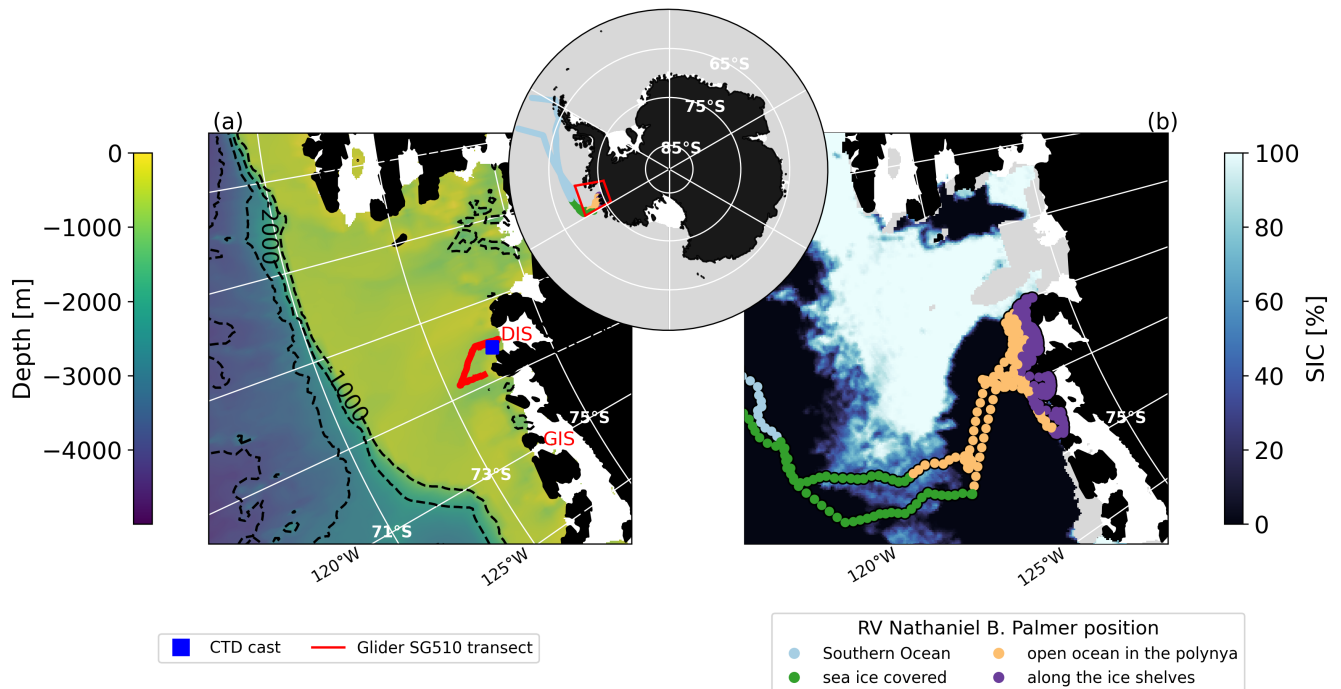90   gridded horizontally per profile and vertically with a resolution of two meters.

Figure 1. (a, b): Antarctica in black, ice shelves from BedMachine (Morlighem et al., 2020) in white. (a): Background is bathymetry from RTopo (Schaffer et al., 2016), the blue square is the CTD cast location used to force the 1D model, in red is the glider transect. Dotson and Getz ice shelves (DIS; GIS) are indicated in red. (b): sea–ice concentration from ASI algorithm on 19 February 2022 (downloaded from https://data.seaice.uni-bremen.de; Spreen et al. 2008), the RV transect is indicated by the scatters colored by the location classification. The red box on the zoomed-out map is the Amundsen Sea plotted on (a, b).

2.1.2   Reanalysis dataset: ERA5

In this study, we assess ERA5 by comparing its hourly mean THF with the THF computed from the observations. We also use some of ERA5's hourly mean meteorological and sea surface variables to recalculate the THF (Table 2). ERA5 is a global reanalysis product that provides "maps without gap" of atmospheric and sea surface variables (Hersbach et al., 2020). It has a hourly temporal resolution and a regular 0.25° lat-lon grid. To co-locate its variables to the ship data, we use the nearest neighbour grid cell and the corresponding hour (as the ship data have been hourly averaged).

Variable	Unit
2 meter temperature	K
SST	K
2 meter dewpoint temperature	K
Wind (zonal and meridional components)	m s^{-1}
Mean surface net shortwave radiation flux	W m^{-2}
Mean surface net longtwave radiation flux	W m^{-2}
Mean surface latent heat flux	W m^{-2}
Mean surface sensible heat flux	W m^{-2}

Table 2. ERA5 variables used in this study

2.1.3 Satellite based data: sea–ice concentration from the ARTIST sea–ice algorithm

We use sea–ice concentration to determine when the research vessel was surrounded by sea–ice (15 % threshold) for the location classification (Fig. 1b). We select the satellite based sea–ice product ARTIST sea–ice (ASI) created by Bremen Uni-
100 versity (Spreen et al., 2008, data downloaded from: https://data.seaice.uni-bremen.de/amsr2). The ASI algorithm takes input data from the Advanced Microwave Scanning Radiometer 2 (AMSR2) (Level 1B) - a sensor operating on the JAXA satellite GCOM-W1 - and outputs gridded data (Level 3, grid space is 3.125 km or 6.25 km). The temporal resolution is daily, the selected output grid space for this study is 3.125 km. The ASI algorithm has been validated against observations and shows good performance (Spreen et al., 2008). It should be noted that during the research cruise, the sea–ice gradually melted, so that
105 from February 2022 onwards, we can no longer really speak of a polynya, as only a tongue of ice attached to the Thwaites ice shelf remains visible in the satellite-derived product (https://data.seaice.uni-bremen.de/databrowser/). We therefore refer to the polynya *region*.

2.2 Methods

2.2.1 Turbulent heat flux computation and analyses: COARE 3.5 algorithm, Reynolds decomposition, and indices of
110 contribution

The THF is the sum of the latent heat flux (LHF) and the sensible heat flux (SHF). The LHF is related to the air–sea heat exchange originating from the sea surface evaporation whereas the SHF arises from the air–sea temperature gradient. We use the Coupled Ocean–Atmosphere Response Experiment (COARE) 3.5 algorithm (Edson et al., 2013) through AirSeaFluxCode (Biri et al., 2023) to compute the THF from the observations. The COARE 3.5 algorithm relies on bulk parameterisations: the
115 LHF and SHF are computed as a function of air density (ρ_{air}), wind speed measured at height z_u (U_{z_u}), transfer coefficient corresponding to the measured height z_m of humidity and temperature and the measured height z_u of wind speed ($C_q(z_m, z_u)$

or $C_t(z_m, z_u)$) and, for the SHF (Eq. (1)), specific heat capacity (C_p), air–sea temperature gradient ($T_{air,z_m} - T_{skin}$); and for the LHF (Eq. (2)), latent heat of vaporization (L_v), air–sea humidity gradient ($q_{air,z_m} - q_{sat}$).

$$SHF = \rho_{air} C_p C_t(z_m, z_u) U_{z_u} (T_{air,z_m} - T_{skin}) \tag{1}$$

120 $$LHF = \rho_{air} L_v C_q(z_m, z_u) U_{z_u} (q_{air,z_m} - q_{sat}) \tag{2}$$

The AirSeaFluxCode applies a logarithmic correction in the transfer coefficient definitions ($C_t(z_m, z_u)$ and $C_q(z_m, z_u)$) to account for the height z_u of wind speed and z_m of air temperature and humidity measurements (Biri et al., 2023). Atmospheric stability is accounted for in the definition of the transfer coefficients C_t and C_q through stability functions. The measured relative humidity is converted to saturated humidity by using saturation vapour pressure function from Buck (2012). Warm

125 layer and cool skin corrections are applied to convert the measured SST (Table 1) to skin SST as required in Eq. (1). These corrections follow Fairall et al. (1996). The COARE 3.5 algorithm requires wind speed relative to the ocean surface. Here, we assume that the ocean currents are low in comparison to the wind speed and neglect them. We find this reasonable as Kim et al. (2016) have shown from recording current meters installed on a two-years mooring that the coastal surface current in the Amundsen Sea is about 0.2 cm s^{-1}, which is 0.03 % of the mean wind speed (7.9 m s^{-1}, Fig. 2a) in our dataset. The flux

130 convention is downward, which means a negative (positive) flux corresponds to a heat loss (gain) for the ocean surface.

To account for the insulating effect of sea–ice we scale the turbulent fluxes by the sea–ice concentration (SIC) when SIC $\geq$ 15 % (Eq. (3), (4) and (5)). We acknowledge that this is a simplified method to account for sea–ice effect on turbulent fluxes, but accept this considering the little time spent by the RV in sea–ice covered area (3 days out of 57) and low importance of the flux variability in sea–ice for the results of this study.

135 $$LHF = (1 - A)LHF \tag{3}$$

$$SHF = (1 - A)SHF \tag{4}$$

where:

$$A = \begin{cases} SIC & \text{if SIC } \geq 0.15 \\ 0 & \text{if SIC } < 0.15 \end{cases} \tag{5}$$

We perform a Reynolds decomposition to analyze the flux variability. We decompose SHF and LHF into the sum of their

140 average (denoted by ‾) and their anomaly (denoted by '): SHF = $\overline{SHF}$ + SHF', and LHF = $\overline{LHF}$ + LHF'. We follow the same

method as in Tanimoto et al. (2003); Chuda et al. (2008); Yang et al. (2016) except that we do not neglect the contribution of C_q' and C_t' as they are more than 5 % of their mean values (not shown; criteria following Cayan, 1992). We replace the variables U_{z_u}, $\Delta T = T_{air,z_m} - T_{skin}$, $\Delta q = q_{air,z_m} - q_{sat}$, C_q and C_t in Eq. (1) and (2) by the sum of their mean and anomaly (details in Appendix B). Finally, we obtain:

SHF' = SHF − $\overline{\text{SHF}}$ =

$$
\rho_{air}C_p\left[\underbrace{\Delta T'\bar{U}\bar{C_t}}_{\text{t-term}} + \underbrace{\overline{\Delta T}U'\bar{C_t}}_{\text{u-term}} + \underbrace{\overline{\Delta T}\bar{U}C_t'}_{\text{ct-term}} + \underbrace{\bar{C_t}(\Delta T'U' - \overline{\Delta T'U'})}_{\text{t-u-term}}\right.
$$

$$
\left. + \underbrace{\bar{U}(\Delta T'C_t' - \overline{\Delta T'C_t'})}_{\text{t-ct-term}} + \underbrace{\overline{\Delta T}(U'C_t' - \overline{U'C_t'})}_{\text{u-ct-term}} + \underbrace{\Delta T'U'C_t' - \overline{\Delta T'U'C_t'}}_{\text{cov-term}}\right] \tag{6}
$$

LHF' = LHF − $\overline{\text{LHF}}$ =

$$
\rho_{air}L_v\left[\underbrace{\Delta q'\bar{U}\bar{C_q}}_{\text{q-term}} + \underbrace{\overline{\Delta q}U'\bar{C_q}}_{\text{u-term}} + \underbrace{\overline{\Delta q}\bar{U}C_q'}_{\text{cq-term}} + \underbrace{\bar{C_q}(\Delta q'U' - \overline{\Delta q'U'})}_{\text{q-u-term}}\right.
$$

$$
\left. + \underbrace{\bar{U}(\Delta q'C_q' - \overline{\Delta q'C_q'})}_{\text{q-cq-term}} + \underbrace{\overline{\Delta q}(U'C_q' - \overline{U'C_q'})}_{\text{u-cq-term}} + \underbrace{\Delta q'U'C_q' - \overline{\Delta q'U'C_q'}}_{\text{cov-term}}\right] \tag{7}
$$

LHF' and SHF' are the flux variability around the mean. We establish indices of contribution for each term of Eq. (6) and (7), following Yang et al. (2016). To quantify the contribution of a term X (X has to be substituted by one of the terms defined in Eq. (6) and (7) to the flux anomaly Y (Y=L for the LHF' and Y=S for the SHF'), we compute the absolute value of the X-term and divide it by the sum of the absolute values of the seven terms (Eq. (8)).

$$
C_Y(X) = \frac{|\text{X-term}|}{\sum|\text{all terms}|} \tag{8}
$$

Therefore the contribution indices $C_Y(X)$ have values between 0 and 1 and their sum equals to 1. The closer to 1 is $C_Y(X)$, the larger the contribution of the term X is to the flux anomaly SHF' or LHF'.

2.2.2 Turbulent heat flux impact on the sea surface temperature and the heat content: 1D-model

The 1D mixed-layer model PWP (Price Weller Pinkel; Price et al., 1986) is used to investigate the relative impact of different THF estimates, produced using observations and ERA5, on the SST and HC. The model needs two input files: one contains the initial ocean state (temperature and salinity profiles), the other contains a time series of the atmospheric forcing (radiative flux, turbulent flux, freshwater flux and momentum flux). The initial ocean profile (Fig. C1) comes from a CTD cast in front of Dotson ice shelf (74.0° S, 113° W), Fig. 1a, blue square. We carry out four simulations with forcings from the observations and ERA5 that differ only in the THF (Fig. C2e, g) in order to isolate its effect. The input freshwater flux only contains precipitation

and evaporation, freshwater input from melting sea–ice was not considered in this study. We consider this reasonable as 2022 was a record-low sea–ice year (Turner et al., 2022; Yadav et al., 2022), and most of the sea–ice melt had already occurred in the polynya region (https://data.seaice.uni-bremen.de/databrowser/). The four simulations are further detailed in Sec. 3.3. We remove the Southern Ocean data to focus on the polynya region. The simulations are accomplished with the aim of: (i)

165 evaluate if the ERA5 flux co-location/computation method is important, (ii) verify if any bias was induced by a moving ship, (iii) retrieve daily change in SST and HC due to THF and compare them to the observations from the glider and the ship. We compute the ocean HC (Eq. (9)) across the upper 40 meters of the water column because all four simulations converge below 40 meters (Fig. 9g). ρ_0 is the mean potential density in the first 40 meters, computed from Absolute Salinity and Conservative Temperature; c_p is the mean specific heat capacity in the first 40 meters, computed from Absolute Salinity, in situ temperature

170 and sea pressure, C_T is the Conservative Temperature.

$$HC = \rho_0 c_p \int_{z=0}^{z=40} C_T dz \tag{9}$$

3 Results

3.1 In situ observations: turbulent heat flux characteristics in the Amundsen Sea

3.1.1 Turbulent heat flux variability: the leading component in the Amundsen Sea

175

First, we analyze the THF computed from the ship observations (Fig. 2) to understand the heat flux magnitude and variability in the Amundsen Sea (Fig. 3).
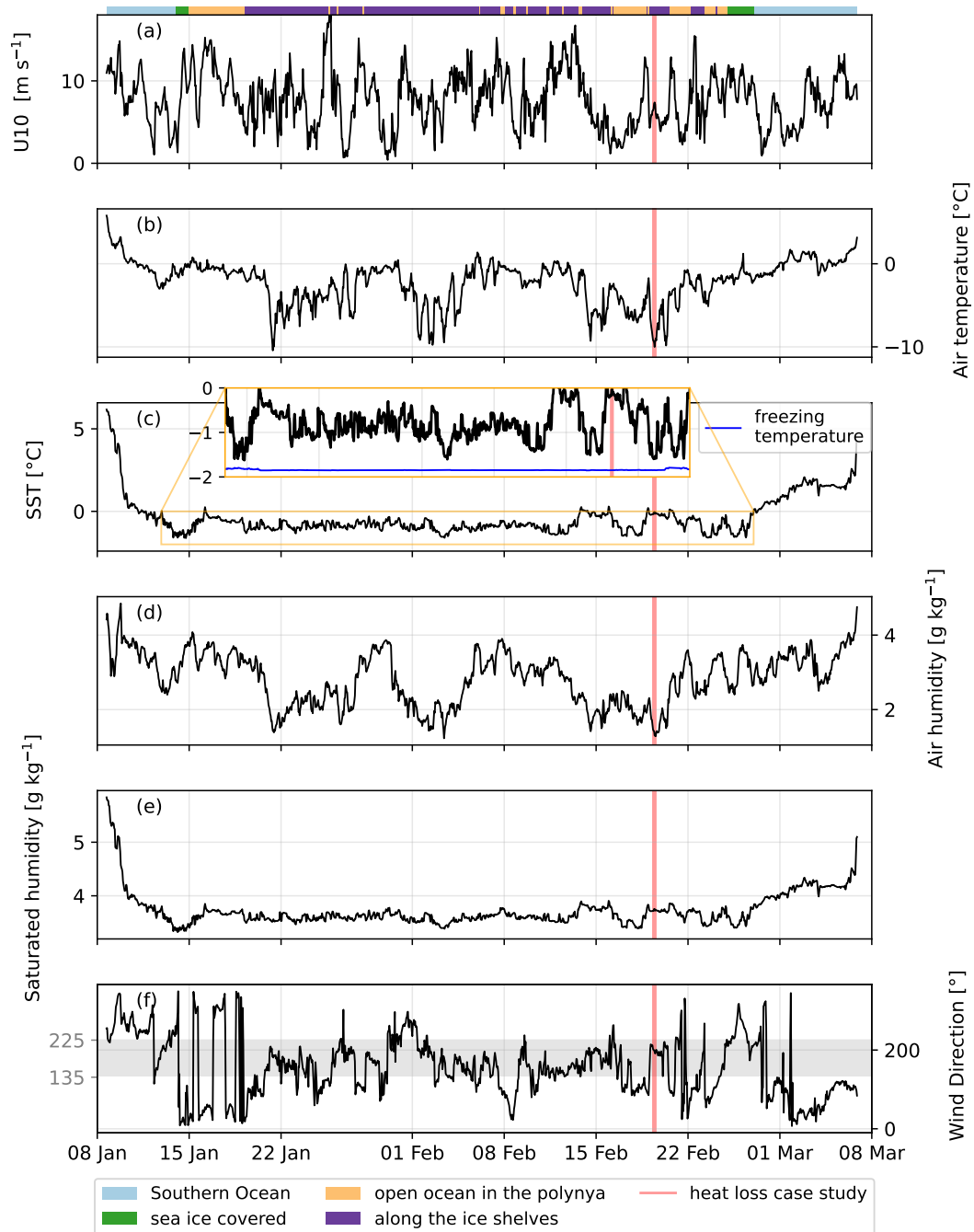
Figure 2. Main sea surface and atmospheric variables. The colors on top of the first time series is the classification of the RV *Nathaniel B. Palmer* position. Note that no sea ice was found near the ice shelf front. The red area is the heat loss event selected for the case study (Sect. 3.1.3). The grey area in (f) represents the wind direction when blowing from 135 to 225° i.e. blowing from the south-west, south and south-east.

The Amundsen Sea (comprising the polynya region and along the ice shelves in the classification) lost on average more turbulent heat (-52 W m^{-2}; STD = 51 W m^{-2}) than the Southern Ocean region (-30 W m^{-2}; STD = 26 W m^{-2}, Fig. 3e). The

180 largest instantaneous heat loss events were also observed in the Amundsen Sea (maximum is -230 W m^{-2} versus -145 W m^{-2} in the Southern Ocean). In particular, more than 97 % of the turbulent heat loss events larger than 150 W m^{-2} occurred when the ship was within 20 km's of Dotson or Getz ice shelves (purple classification, Fig. 3).
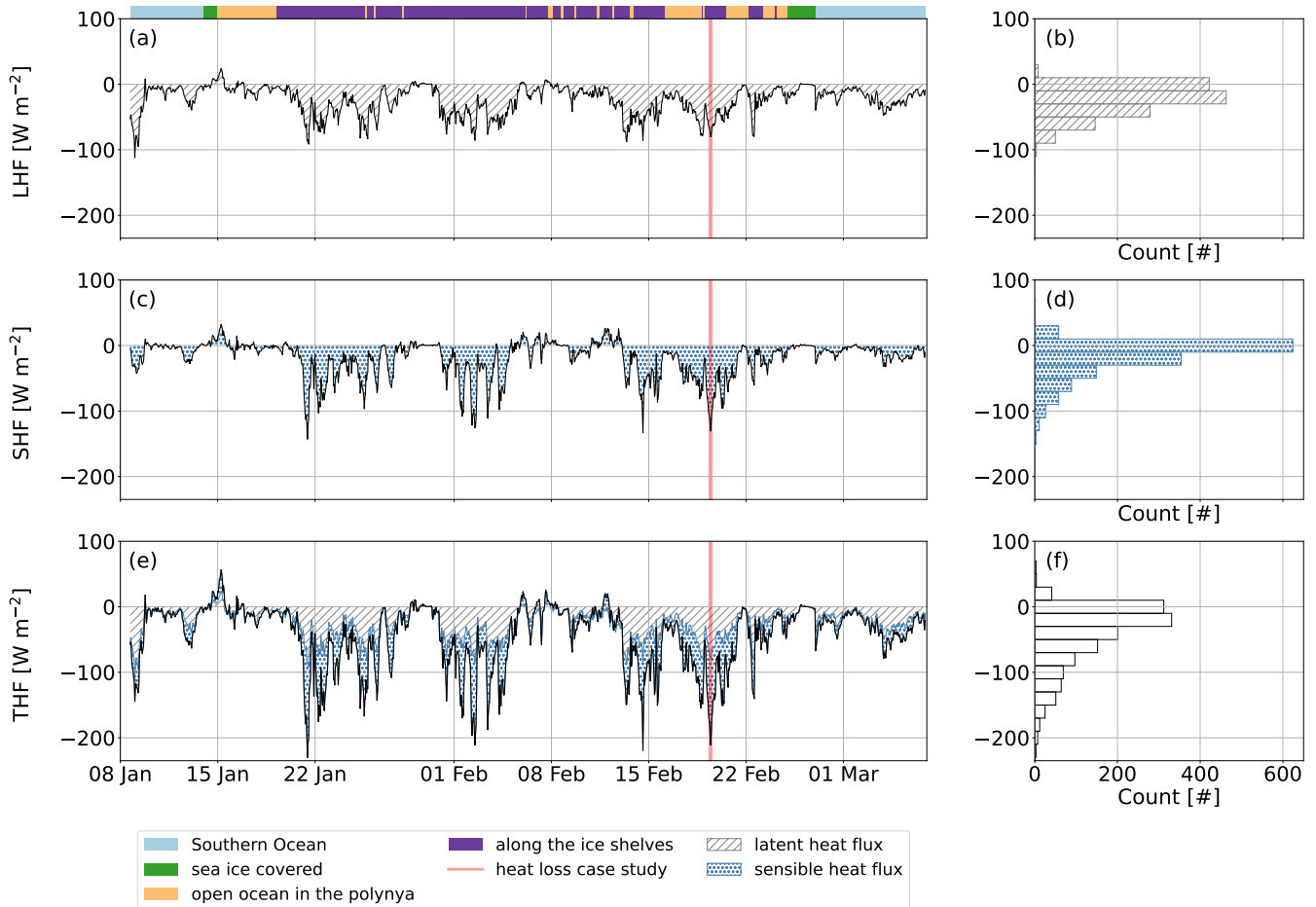
Figure 3. Ship observations of (a, b): latent heat flux ; (c, d): sensible heat flux ; (e, f) the sum of the two: the turbulent heat flux. A positive heat flux is a gain by the ocean (downward convention). The colors on top of the first time series and the red area are as in Fig. 2.

Within the polynya region, the THF variations (Fig. 3e) were linked to short-scale SHF loss between -90 and -140 W m^{-2} (Fig. 3c), while in the Southern Ocean, the largest turbulent heat loss events (Fig. 3e) were driven by the LHF loss (Fig. 3a).

185 Throughout the time series, the LHF contributed most to the net THF loss, accounting for an average of 57 % of the THF. This is evidenced by the mode of both the LHF and THF being between -30 and -10 W m^{-2}, whilst for the SHF the mode is

11

between -10 and 10 W m^{-2} (Fig. 3b, d, f). Thus, while the LHF contributed the most to the total THF, the most significant short-term (days to weeks) THF loss events were imputed to large SHF losses.

3.1.2 Turbulent heat flux decomposition: enhanced air–sea temperature and humidity gradients responsible for large episodic heat loss events

Below, we investigate the key drivers in the variability of the THF. We decompose the flux anomalies into different terms (Eq. (6), (7)). These terms indicate the contribution of the temperature gradient (t-term), humidity gradient (q-term), wind speed (u-term), transfer coefficients (ct-term and cq-term), and the cross-contribution of these variables: second-order terms (t-u-term, q-u-term, u-cq term, etc) and third-order term or residual (covariance-term) to SHF' and LHF' (Fig. 4).
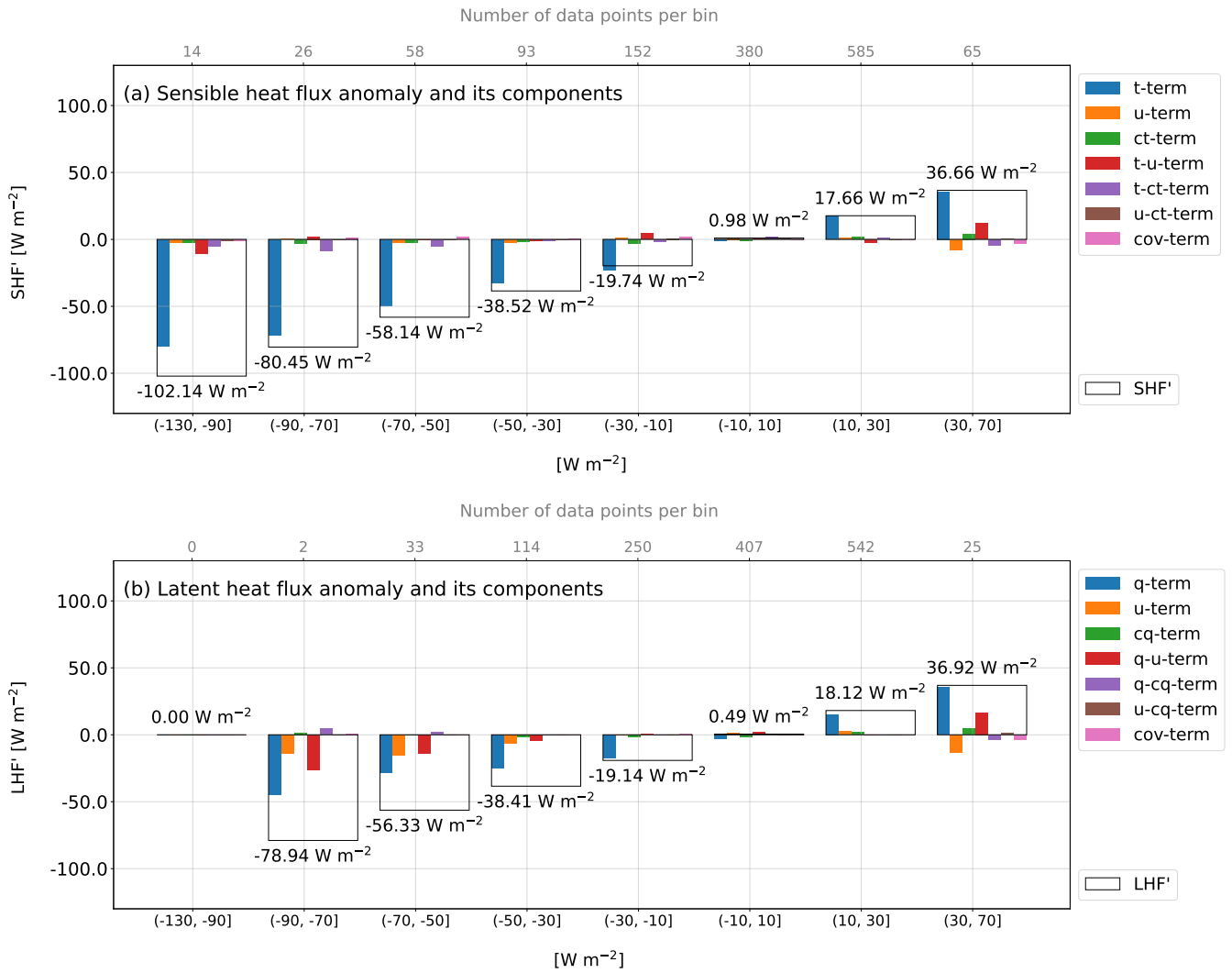
Figure 4. (a) mean SHF' and (b) mean LHF' in black rectangles binned by 20 W m^{-2} or 40 W m^{-2} (for the first and the last bins). The numbers outside of the black rectangles are the mean values of the SHF' (a) and LHF' (b) for the corresponding bin. The colored bars inside the black rectangles are the different terms from Eq. (6) and (7). Their sum gives SHF' and LHF'.

The t-term (associated with the anomalous air–sea temperature gradient) was larger than the sum of all the other terms, (Fig. 4a, blue colorbars dominate). The indices of contribution of the terms (Table 3) were calculated for each hourly data and range between 0 and 1 to show the relative importance of one term compared to another. The t-term was the most frequent dominating factor: 37 % of C_S(t) values were above 0.5 (Table 3). This indicates that in 37 % of the data, air–sea temperature gradients were responsible for more than 50 % of SHF'. Following the same arguments, the q-term (anomalous air–sea humidity gradient)

13

contributed the most to LHF' (Fig. 4b - blue colorbars), but to a slightly lesser extent: above 33 % of LHF' values had $C_L(q)$ as the strict dominant factor.

$C_S(X)$	$C_S(t)$	$C_S(u)$	$C_S(ct)$	$C_S(t-ct)$	$C_S(t-u)$	$C_S(u-ct)$	$C_S(cov)$
Median	0.43	0.17	0.06	0.09	0.16	0.02	0.04
IQR	0.29	0.26	0.04	0.09	0.10	0.03	0.02
% values > 0.5	37.22 %	1.75 %	0 %	0 %	0 %	0 %	0 %
$C_L(X)$	$C_L(q)$	$C_L(u)$	$C_L(cq)$	$C_L(q-cq)$	$C_L(q-u)$	$C_L(u-cq)$	$C_L(cov)$
Median	0.40	0.22	0.08	0.07	0.12	0.03	0.03
IQR	0.28	0.19	0.08	0.07	0.09	0.04	0.02
% values > 0.5	33.21 %	7.36 %	0 %	0 %	0 %	0 %	0 %

Table 3. Median and interquartile range (IQR) on the indices of contribution of the seven terms of the Reynolds decomposition. $C_L(X)$ is the contribution of the variable anomaly X to LHF', $C_S(X)$ is the contribution of the variable anomaly X to SHF'. An indice of contribution higher than 0.5 means that the term is the strict dominant factor.

The decomposition indicates that the variability of the air–sea property gradient was the dominant factor impacting the variations of the THF. Further investigations show that the atmospheric variables (air temperature and humidity) control the air–sea property gradients. Indeed, the variability of the air temperature is higher (standard deviation (STD) = 2.62 °C) than the variability of the SST (STD = 1.13 °C), Fig. 2b, c. The same statement holds for the humidity: the air humidity has a higher variability (STD = 0.70 g kg^{-1}) than the saturated humidity (STD = 0.32 g kg^{-1}), Fig. 2d, e. The difference of STD is even larger when we remove the Southern Ocean data (not shown). These results indicate the importance of cold dry air mass driving large heat loss events.

3.1.3 Case study of the heat loss mechanism in the Amundsen Sea: cold and dry southerlies trigger the heat loss

To further analyze the heat loss mechanism in the Amundsen Sea, we investigate the relationship between the turbulent heat loss and the broader scale synoptic variability (Fig. 5).
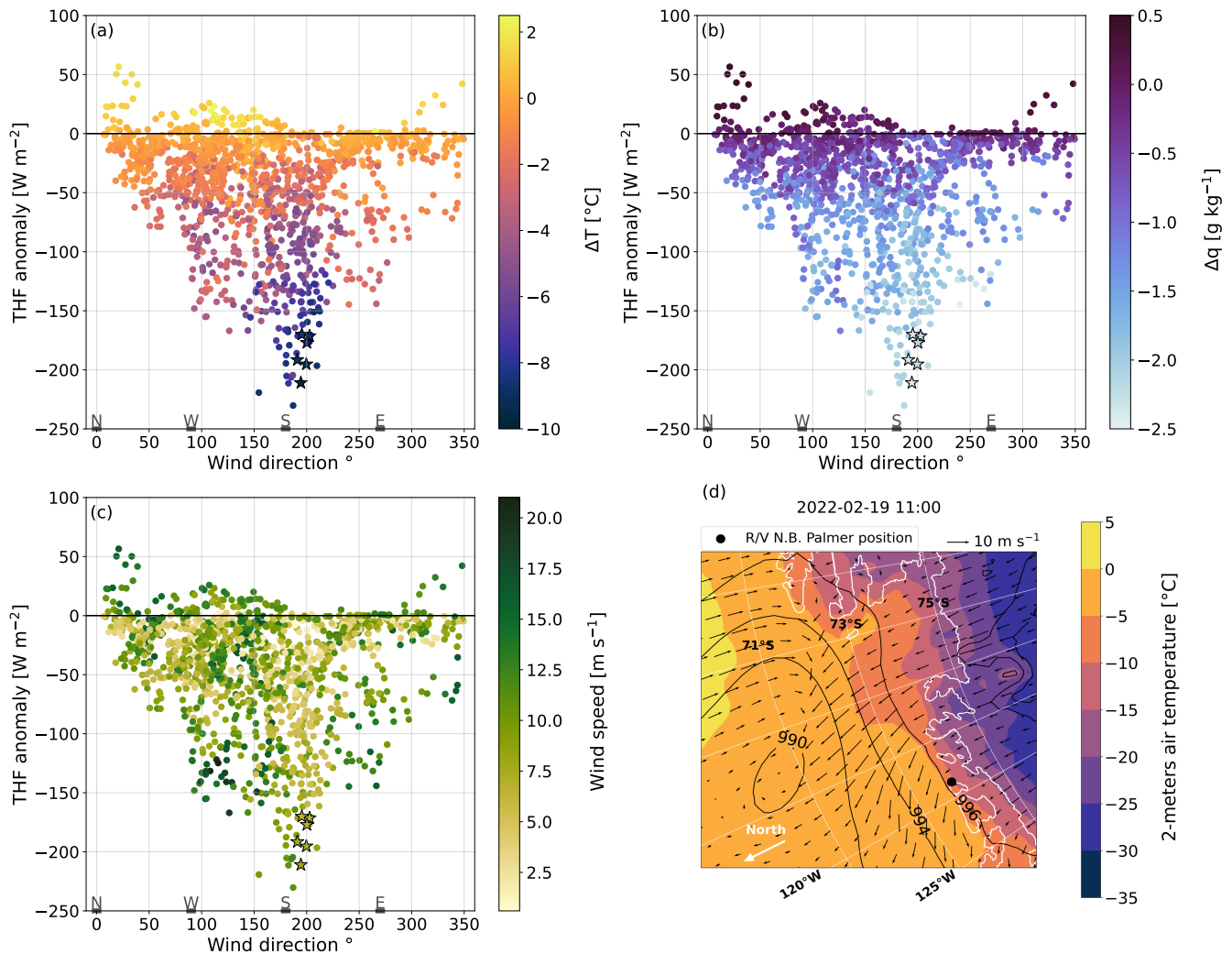
Figure 5. (a–c): THF plotted by the wind direction colored by: (a) the temperature gradient, (b) the humidity gradient or (c) the wind speed. The stars correspond to the heat loss event studied and depicted on map (d). (d) is the Amundsen Sea, the coastline is in white. The black dot is the research vessel position on 19 February 2022. For the same day at 11:00, and from ERA5, are plotted the 10 meters wind speed and direction (arrows), the 2 meters air temperature (background), the isobars (black contour).

The large turbulent heat losses were associated with winds blowing from the south (Fig. 5a, b, c) with large temperature Fig. (5a) and humidity (Fig. 5b) gradients. We focus on one heat loss event that lasted six hours on 19 February 2022 from 08:00 to 13:00 (stars on Fig. 5). The THF remained below -170 W m^{-2} (Fig. 3, red area), reaching its peak of -211 W m^{-2} at 11:00. The mean value over the 6 hours was -186 W m^{-2}. The wind was directed from the continent (Fig. 5d wind vectors, and Fig. 2f) and brought cold (on average -9.4 °C, Fig. 2b) and dry (1.4 g kg^{-1}, Fig. 2d) air on top of the warmer (on average -0.1 °C, Fig. 2c) and moister (3.7 g kg^{-1}, Fig. 2e) sea: triggering the heat loss event. A low pressure center was also visible on the map

(Fig. 5d). It may have enhanced the heat loss event. This weather system (cold and dry continental winds) has been observed for all the major turbulent loss events occurring during this research cruise (not shown). Contrariwise, the instances when the THF was significantly positive (> 30 W m^{-2}) are consistent with warm and moist northerlies blowing over the Amundsen Sea (Fig. 3e and Fig. 2f).

This indicates the role of large scale atmospheric variability on the local flux events. Next, we review start-of-the-art reanalysis to understand the ability of numerical weather models to represent these key processes.

3.2 ERA5 reanalysis: revealing the product bias in the Amundsen Sea

3.2.1 Turbulent heat flux bias at land–sea boundaries

The research vessel spent 72 % of its time in the polynya region and along the Dotson and Getz ice shelves where few validations of ERA5 have been conducted. First, we analyze the THF from ERA5 by comparing them to the observed fluxes, calculated using the COARE 3.5 algorithm (Fig. 6).
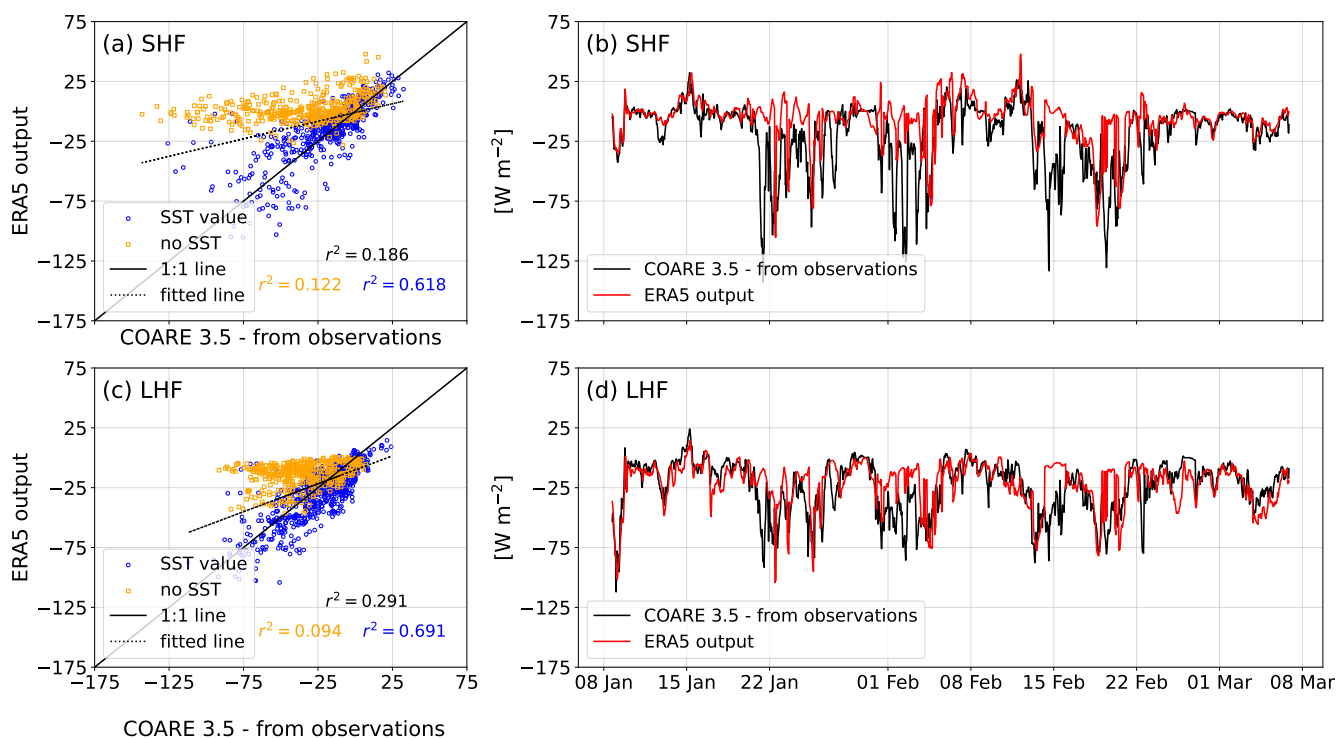

Figure 6. (a, b): SHF and (c, d): LHF. (a, c) are colored by a SST mask (in blue the data points where the ERA5 cell has a SST value, in yellow where SST is NaN: these points are then classed as ice shelf). The r^2 in black is the coefficient of determination for all the scatters, the r^2 in blue and in yellow are the coefficients of determination of the scatters corresponding to the SST mask. (b, d): the black lines are the fluxes computed from the research vessel measurements with the COARE 3.5 algorithm, in red are fluxes from ERA5. ERA5 fluxes are co-located to the research vessel position by selecting the nearest ERA5 value.

16

The agreement between THF product from ERA5 and the THF calculated from in situ data via COARE 3.5 was low; $r^2 = 0.186$ for the SHF (Fig. 6a) and $r^2 = 0.291$ for the LHF (Fig. 6c). Additionally, ERA5 was positively biased in comparison to the observations: the mean SHF and LHF were higher by 13 and 3 W m^{-2} (Table 4, 1st and 2nd rows). Similarly, hourly episodic heat loss events were not well represented by ERA5 (Fig. 6b, d): the difference between the two time series was up to 141 W m^{-2} for the SHF and 81 W m^{-2} for the LHF (Table 4, 2nd row).

Flux product	mean SHF	mean LHF	SHF max diff.	LHF max diff.	RMSE SHF	RMSE LHF
observation-based	-20 W m^{-2}	-25 W m^{-2}	-	-	-	-
ERA5 output	-7 W m^{-2}	-22 W m^{-2}	141 W m^{-2}	81 W m^{-2}	29 W m^{-2}	20 W m^{-2}
ERA5 from hybrid dataset	-23 W m^{-2}	-29 W m^{-2}	107 W m^{-2}	69 W m^{-2}	21 W m^{-2}	14 W m^{-2}

Table 4. Comparison of the different flux products. The LHF and SHF max diff. are the maximum absolute difference between the flux from the in situ observations and another flux product (either the ERA5 fluxes or the ERA5 hybrid fluxes). RMSE is the root mean square error.

The low agreement between the two flux products is explained by the coarse resolution of ERA5 at land–sea boundaries. The research vessel was often stationed along the ice shelves where the ERA5 closest grid cell was considered as ice shelf, and as such does not have a SST value (Fig. 7). The correlation between ERA5 and the COARE 3.5 fluxes improved when only comparing instances where the nearest ERA5 grid cell had a SST value not set to NaN ($r^2 = 0.618$ for the SHF and $r^2 = 0.691$ for the LHF, Fig. 6a, c, blue scatters). For instances where there is no SST, the correlation is weak ($r^2 = 0.122$ for the SHF and $r^2 = 0.094$ for the LHF, same Figure, sub-panels, yellow scatters). Thus, the ERA5 reanalysis THF product underestimates the turbulent losses at the land–sea boundary formed by the ice shelves due to missing SST values. These results illustrate the importance of careful analysis when investigating ice shelf processes in reanalyses.
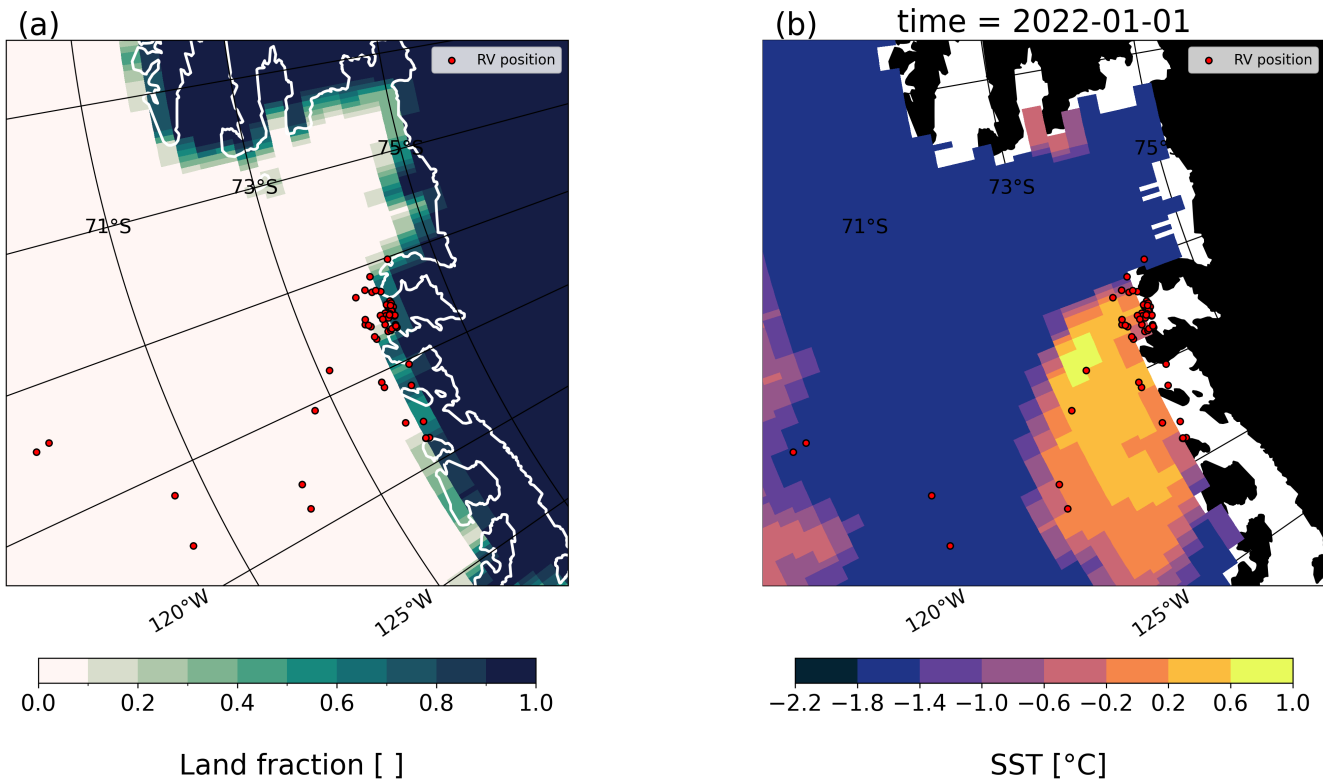
Figure 7. (a) Land–sea mask from ERA5 and (b) SST from ERA5. Research vessel position plotted every 18 hours (red scatters).

3.2.2 A hybrid dataset to reduce the bias

As shown above, the dominant mechanism impacting the THF was the variations in air temperature and humidity. As such, to make use of all available ship based observations to compare with ERA5, we require more suitable method to reduce the SST-based biases identified. We considered using the nearest THF that is an ocean point, but this method was not chosen as this would induce a bias in the THF magnitude caused by an overestimation of air temperature (not shown).

We create an ERA5 dataset with the atmospheric variables (wind, air temperature, dew-point temperature, pressure) co-located using the closest ERA5 value, and with the SST co-located using the closest cell that has a SST value. We found this reasonable as the SST variability is less important (range = 1.9 °C) than the air temperature (range = 12.2 °C) in the polynya region during the research cruise (Fig. 2b, c). Therefore the gradient of temperature in Eq. (1) mainly depends on the air temperature. The COARE 3.5 algorithm was then applied to compute turbulent fluxes using the new dataset as input (Fig. 8). We refer to the original ERA5 THF product as the "nearest neighbour product", which suffers from an innacurate landmass, and the new product calculated from ERA5 atmospheric variables and valid SST as the "hybrid product" (hybrid because of the difference of co-location method between the SST and the other variables).
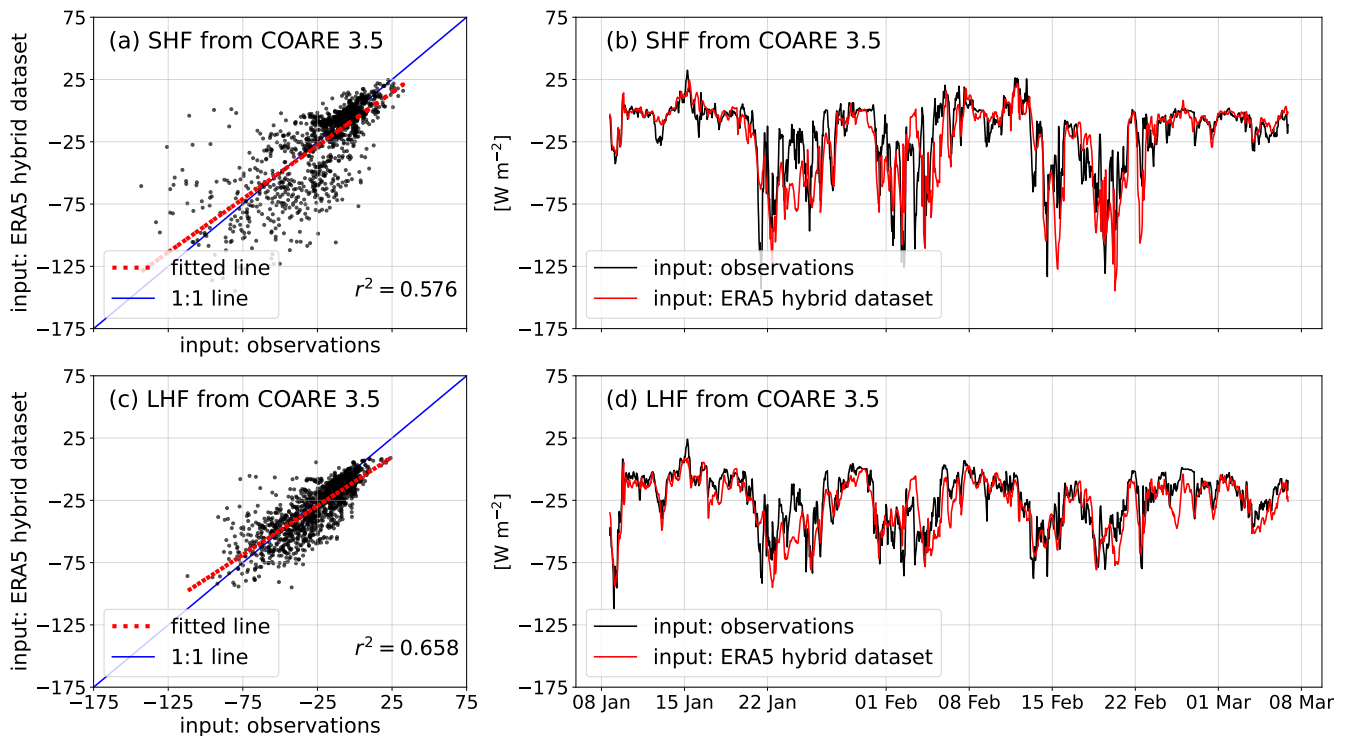
Figure 8. (a, b): SHF, (c, d): LHF from COARE 3.5 algorithm with input from ERA5 hybrid dataset (in red) and input from RV *Nathaniel B. Palmer* measurements (in black).

The SHF correlation between ERA5 and the observations was higher with the ERA5 hybrid dataset ($r^2 = 0.576$, Fig. 8a) than the original nearest-neighbour dataset ($r^2 = 0.186$, Fig. 6a). The same statement holds for the LHF: $r^2 = 0.658$ for the hybrid dataset (Fig. 8c) versus $r^2 = 0.291$ for the nearest-neighbour flux (Fig. 6c). The hybrid SHF was on average closer to the observations-based fluxes (lower by 3 W m^{-2}, Table 4) but with a negative bias because of colder air–temperature (Fig. D1c). Regarding the mean LHF, the hybrid dataset did not bring a clear improvement: the mean hybrid SHF is lower by 4 W m^{-2} than SHF from observations whereas the mean ERA5 SHF output was higher by 3 W m^{-2}. The instantaneous heat loss was slightly better represented (Fig. 8b, d in comparison to Fig. 6b, d) with a maximum difference between the time series of 107 W m^{-2} for the SHF and 69 W m^{-2} for the LHF (Table 4).

3.3 1-D model simulations and glider data: determining the importance of an accurate turbulent heat flux estimate

We understood the characteristics of the heat loss events in the Amundsen Sea (Sect. 3.1) and evaluated ERA5 in this region (Sect. 3.2). We found an underestimation of the turbulent heat loss from ERA5 THF output, and we created a hybrid ERA5 dataset that overestimates the heat loss but fits better the observations. In this last section we evaluate the impact of the THF on the SST and HC variability. More specifically, we determine whether the overestimation (or underestimation) of ERA5 fluxes is critical for estimates of SST and HC. We use a 1-D model to answer these questions. We ran four PWP simulations with

different atmospheric forcing that differed only in their THF (Fig. C2e, g and Fig. 9a). Three out of the four THF products were used earlier in this study: the THF computed from the research vessel via COARE 3.5 ("observation dataset"), the ERA5 THF co-located using the nearest-neighbour approach (suffering from the land–mask issue) and the THF computed from the ERA5 hybrid dataset via COARE 3.5. The last THF is obtained directly from ERA5 at a single ocean grid cell so as to represent the time varying dynamics and exclude any lateral processes associated with a moving ship. We call this the stationary dataset.

3.3.1 Turbulent heat flux effect on sea surface temperature

The PWP model predicted a warming of the water column over the 35-days for all four simulations (Fig. 9g), which is in agreement with the seasonal warming expected during the austral summer. However, the SST of the four PWP simulations diverge (Fig. 9c). At the end of the 35-days run (duration of the expedition in the polynya region), the nearest-neighbour SST (darker red line) was higher (0.76 °C, Fig. 9e) than the other three simulations. The hybrid (middle-red line) and stationary (lighter red line) simulations were colder (-0.17 °C and -0.14 °C) than the observation simulation (black line in Fig. 9c). This is in agreement with the ERA5 overestimation of heat loss for the hybrid dataset and underestimation for the nearest-neighbour dataset. The HC in the 40-meters upper layer was higher by 8.2×10^7 J at the end of the 35-days for the nearest-neighbour simulation, and lower by -3.30×10^7 J and -2.98×10^7 J for the hybrid and stationary simulations (Fig. 9f) in comparison to the observation-based simulation.
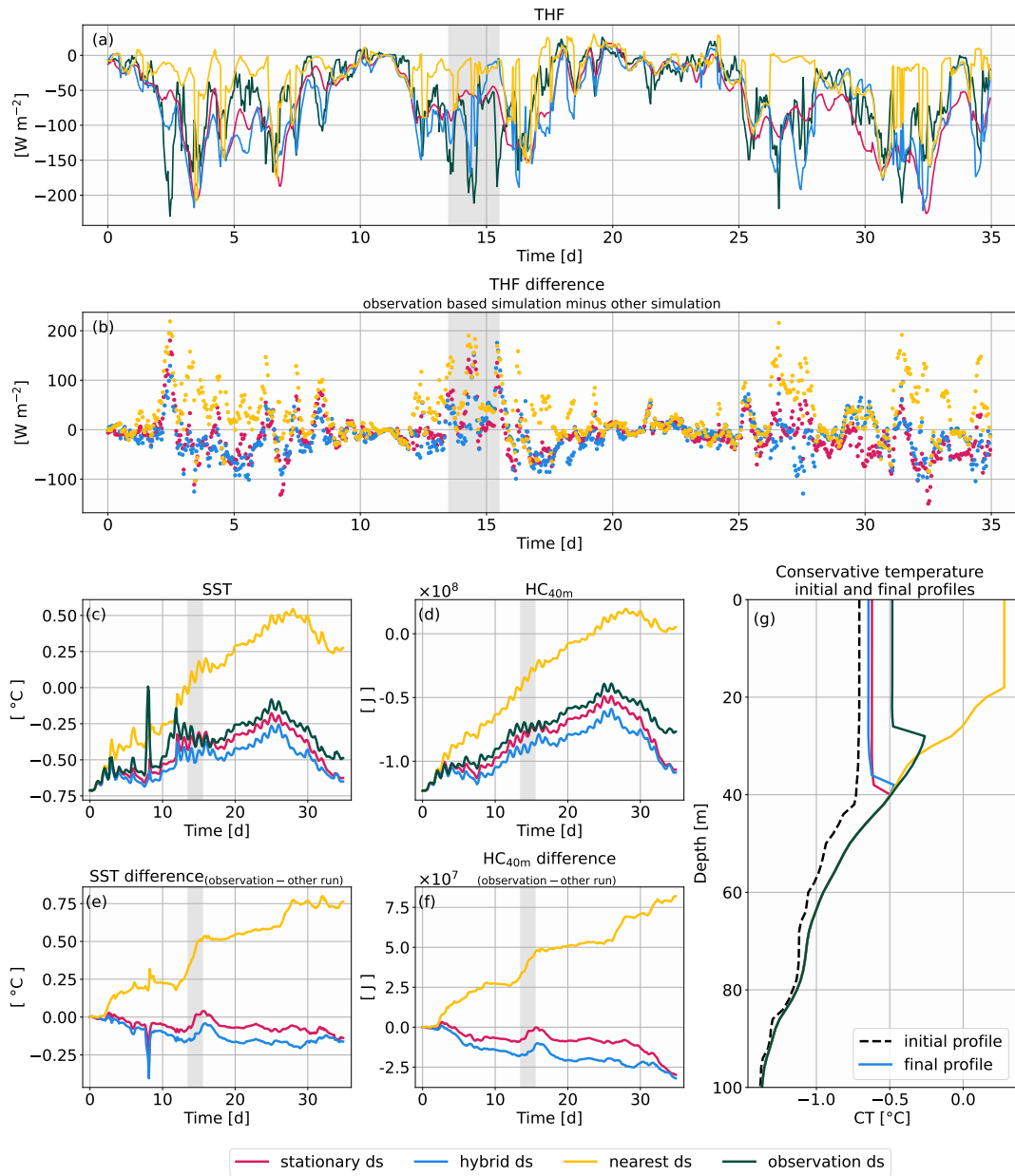
Figure 9. (a) THF input for the PWP model, (b) THF difference for the observation based simulation minus one of three other simulations. (c) SST model output and (d) HC in the upper 40-meters layer computed from the model's output. (e) and (f) are the difference of SST and HC between the observation-based run and the other runs. (g) shows the initial temperature profile (dotted line) and the final temperature profiles. The grey shaded area on all the panels corresponds to a two-days period that we examine in the results.

The observation and the nearest-neighbour simulations had large THF difference (on average 28 W m^{-2} and instantaneously up to 200 W m^{-2} ; Fig. 9b, dark red scatters) that led to an increase in the slope of the difference of SST (Fig. 9e) and HC

285

(Fig. 9f) between the two simulations. For example, from day 13.5 to day 15.5 (grey shaded area), the nearest-neighbour THF was on average 82 W m^{-2} warmer than the observed THF. This difference explained a SST increase of 0.20 °C and a HC increase of 1.4×10^7 J (dark red line, Fig. 9e, f) of the nearest-neighbour simulation in comparison to the observation-based simulation. The cumulative effect of such events is critical in setting the SST and HC differences between the simulations

290 throughout the 35-days simulations (Fig. 9e, f).

We note that the daily change in SST (ΔSST, Table 5) has the same order of magnitude between the stationary dataset-based simulation (mean = 0.003 °C d^{-1}, STD = 0.042 °C d^{-1}) and the hybrid dataset-based simulation (mean = 0.002 °C d^{-1}, STD = 0.040 °C d^{-1}), which gives us confidence in the credibility of using the PWP model with data that are not stationary (i.e. biases introduced when comparing datasets from moving vessels).

295 Thus, the four simulations diverge because of the different THF inputs (indeed all the other atmospheric forcings are identical). The resulting difference in evolution of SST (HC) of 0.76 °C (8.2×10^7 J) over a month is not negligible for a coastal polynya region where sea–ice formation and melting, ice shelf melting and primary production are dominant processes.

3.3.2   A sea surface temperature and heat content bias as large as the spatial-scale variability

In this final subsection, we look at ship-based thermosalinograph data (TSG) (for the SST) and nearby glider data (for the HC)
300 to understand how the temperature change in the PWP simulations compare to the change of temperature in the observations.

ΔSST from the PWP model output (solid lines, Fig. 10a) and from the TSG observations (dotted line) showed a similar average change (Table 5 ; mean: $O(10^{-3})$ °C d^{-1}), except for the nearest-neighbour PWP output that has a higher mean (0.029 °C d^{-1}). Regarding the HC, the nearest-neighbour simulation exhibits a higher mean as well, even though the difference is smaller than for the SST (Table 6). STD of the daily change of SST and HC are one order of magnitude higher for the
305 observations (0.140 °C d^{-1}, 2.0×10^7 J d^{-1}) than for the model outputs ($O(10^{-2})$ °C d^{-1}, $O(10^6)$ J d^{-1}), Tables 5 and 6. The larger spread in the observations can be explained by the horizontal processes that are assumed to be non-negligible in a sea-shelf environment, and that were not represented in the 1D model.

It is thus reasonable to assume that the horizontal processes average out (as seen by the comparison of the means), the 35-days evolution of SST and HC in the observations was well represented by the PWP simulations, the nearest-neighbour
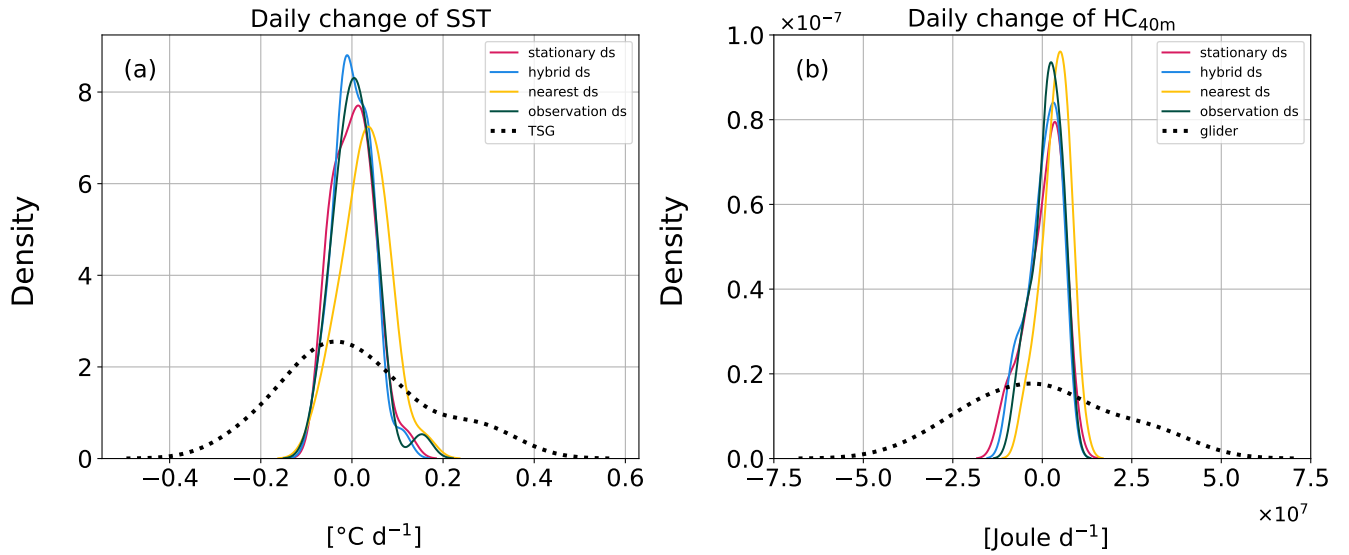310 simulation set aside.

Figure 10. Distribution of: (a) the daily change of SST and (b) the daily change of HC in the upper 40-meters layer for the four PWP simulations (continuous line) and the observations (dotted line). For the observations, we used ship-based data at 6 meters for the SST and glider data for the HC.

Dataset	Mean ΔSST [°C d^{-1}]	STD ΔSST [°C d^{-1}]
TSG	0.010	0.140
PWP output - obs.	0.007	0.046
PWP output - hybrid	0.002	0.040
PWP output - nearest	0.029	0.049
PWP output - stat.	0.003	0.042

Table 5. Statistics of the change of temperature $\Delta SST = SST_{t_{i+1}} - SST_{t_i}$ with $t_{i+1} - t_i = 1$ d. STD is the standard deviation. The SST is taken at depth = 6 meters for the PWP model to match the depth of the TSG measurements.

Dataset	Mean ΔHC [J d^{-1}]	STD ΔHC [J d^{-1}]
Glider	4.9×10^5	2.0×10^7
PWP output - obs.	1.4×10^6	3.8×10^6
PWP output - hybrid	5.3×10^5	4.2×10^6
PWP output - nearest	3.8×10^6	3.6×10^6
PWP output - stat.	6.1×10^5	4.7×10^6

Table 6. Same as previous table but statistics of the daily change of heat content in the upper 40-meters layer.

Coming back to the two-days example of the previous section, according to the PWP model we see a misrepresentation of the THF of about 80 W m^{-2} (Fig. 9b) that lead to a SST increase of 0.2 °C (Fig. 9e) and a HC increase of 1.4×10^7 J (Fig. 9f). Across this particular heat loss event, these SST and HC increase was of the same order of magnitude as the spatio-temporal variability scale observed in the 35-days ship-based SST observation (STD = 0.140 °C d^{-1}, Table 5, Fig. 10a) and 18 days glider data (STD = 2.0×10^7 J d^{-1}; Table 6, Fig. 10b) that were imputed to horizontal processes. Therefore, the cumulative effect of small differences in the mean ΔSST and ΔHC due to a bias in the THF is critical for the temporal-scale variability of SST and HC in the Amundsen Sea. 1D processes alone cannot explain the change of SST and HC that we see in the observations. However, our work highlights that a consequent bias in the THF can lead to errors in the estimation of the 35-days evolution of the SST and HC that are of the same order of magnitude of the variability due to horizontal processes.

4 Discussion and conclusions

This work provides the first air–sea THF observation-based study in the Amundsen Sea. Large scale cold and dry winds moving from the Antarctic continent over the sea enhance the air–sea temperature and humidity gradients and trigger turbulent heat loss events up to 230 W m^{-2}. We show that THF from ERA5 are inaccurate at ice shelf boundaries (mean underestimation of the heat loss of 28 W m^{-2} over the 35-days of the research survey in the polynya region). This can be improved by recalculating fluxes from ERA5 sea surface and atmospheric variables, with vigilance regarding the SST that is sometimes set to NaN due to ERA5 land–sea mask. The THF obtained is overestimating the heat loss by 12 W m^{-2} on average in the polynya region. As a result of misrepresenting the THF, we show that the seasonal evolution of the modelled SST would be overestimated (+ 0.76 °C at the end of the 35-days PWP simulation) with ERA5 THF, or underestimated (- 0.17 °C) with ERA5 recalculated flux. Therefore, caution has to be made when selecting turbulent fluxes for modelling studies in a coastal polynya where, for example, sea–ice formation and melting and primary production are important processes.

4.1 Polynya turbulent flux system

4.1.1 The role of the broad atmospheric system

Antarctica is known for its strong surface winds. It might be plausible that the wind contributes significantly to the heat loss by increasing turbulent mixing, yet we did not observe any pattern of increasing wind intensity related to the heat loss (Fig. 4 and Fig. 5c). A systematic positive bias in the residuals was observed in Fig. A1 meaning that either ERA5 underestimates the wind speed or the measurements overestimate it. We imputed the residual bias to ERA5 as it has been shown that the wind speed along Antarctica coastline is underestimated by ERA5 (Caton Harrison et al., 2022). The properties of the air (cold and dry) transported by the winds are more important for the THF variability than the wind speed itself. As shown, the atmospheric system is thought to be a key component in the Amundsen Sea. Indeed, Jones (2018) used the MetUM model to perform episodic (2 to 3 days) high heat flux study cases in the East Amundsen Sea and found that strong easterlies and southeasterlies associated with cyclones are typically linked to heat loss. The importance of low pressure systems in cold air outbreaks is a result that has also been found in the Ronne polynya (Weddell Sea) from aircraft observations (Fiedler et al., 2010). The Amundsen Sea is known for being a cyclogenesis region and we indeed saw recurring low pressure centers in our study area (Fig. 5d). In particular the Amundsen Sea Low (ASL) is a quasi stationary low pressure center that oscillates between the Ross Sea (to the West) and the Bellingshausen Sea (to the East). Hosking et al. (2013) showed that the ASL influences the meridional component of the large scale atmospheric circulation. When the ASL is positioned to the west, it enhances the southerly flow. The ASL was located at the edge of the Ross and Amundsen Sea (to the west) in January and March 2022 and in front of Thurston Island, in the Amundsen Sea, in February 2022 (the ASL index position was downloaded from https://github.com/scotthosking/amundsen-sea-low-index). The ASL had therefore likely enhanced the southerly (continental) winds over the time span of the research vessel presence in the Amundsen Sea, and consequently increased the turbulent heat loss through enhanced air–sea temperature and humidity gradients. It would be interesting in future studies to investigate the longer-term air–sea THF variability associated with ASL locations.

4.1.2 Spatial variability of the fluxes

In this study, the largest heat losses occurred in front of the ice shelves. This result could indicate that the heat loss is larger along the ice shelves than in the open water in the polynya, but could also be explained by the fact that the research vessel spent 27 days out of 41 in front of the ice shelves when being in the polynya region. However, it has been shown by modelling studies in other coastal polynyas (Renfrew et al. 2002, polynya that forms off the Ronne Ice Shelf (Weddell Sea) and Jones 2018, Pine Island Glacier polynya, Pope Smith Kohler polynya and Thurston polynya (Eastern Amundsen Sea)) that the THF decreases with fetch. When continental cold (dry) air is advected on top of the sea, it gains heat (moisture) from the ocean as it travels offshore, which reduces the gradient of temperature (humidity) and as the consequence the SHF (LHF). This result gives us confidence regarding the spatial variability observed in our dataset and illustrates the key mechanisms for driving heat loss in regions of ice shelf dynamics.

4.2 Assessing ECMWF turbulent heat flux in the Amundsen Sea

From ERA-Interim data, Papritz et al. (2015) created a CAO climatology. They found that the CAOs summer frequency is under 3 %, and consequently focused on the nonsummer months. In autumn winter and spring, they found that the CAOs contribute to the turbulent heat loss enhancement. Their study focused on the region of the Amundsen Sea off the ice shelves, and therefore were not affected by the along-shelf dynamics assessed in our study. Yet, we found the same result regarding the importance of CAOs along the ice shelves as the air was cold and dry enough to enhance the air–sea temperature and humidity gradients despite it being summertime. Jones et al. (2016) evaluated the performance of four reanalysis products in the Amundsen Sea, and showed that ERA-Interim has a cold bias in the air temperature and a dry bias in the specific humidity, which is greater near the ice shelves and weaker far from the coast. As a consequence, they hypothesize that the heat loss would be overestimated. This hypothesis has been verified in our work with the bias found (Table 4) in ERA5 hybrid fluxes (computed from the atmospheric and sea surface ERA5 variables). This bias indeed arises from cold and dry biases in ERA5 air and humidity (Fig. D1b, c). However, the ERA5 nearest-neighbour THF underestimates the heat loss: this result indicates the importance of careful choice regarding the method used to retrieve estimates of turbulent flux in the Amundsen Sea from ERA5.

4.3 Implications

The Amundsen Sea is a dynamic shelf sea with horizontal processes such as coastal currents. Therefore the 1D PWP model does not aim to reproduce the observed temperature changes. However, we use the PWP model to give an insight on the potential effects of an air–sea THF misrepresentation on the monthly evolution of SST in the Amundsen Sea. The stationary heat flux simulation and the hybrid simulation show similar results. This indicates that the large scale nature of the CAOs, which drive the strongest fluxes, negate any bias that might have been induced by simulating a 1D model using flux data from a moving ship. In the nearest neighbour simulation, which includes the strongly biased THF, there is a non-negligible impact with the overestimation of SST (+ 0.76 °C) and HC (8.2×10^7 J) at the end of the 35-days simulation. Yu et al. (2023) have shown that the climatological January SST ranges between -0.8 °C and -0.2 °C in the Amundsen Sea Polynya (it has an internal spatial variability), with an interannual standard deviation between 0.35 °C and 0.45 °C. The SST from the hybrid, stationary and observation simulations are therefore in the expected range unlike the nearest neighbour simulation (Fig. 9c). This could have a major impact regarding sea–ice formation or primary production studies as the sea–ice concentration variability is influenced by the SST in summer (Kumar et al., 2021), and the chlorophyll-a concentration correlated to the SST in the Amundsen Sea (Garcia et al., 2021).

The Amundsen Sea polynya has high rates of primary production that are driven both by the polynya duration and by the iron supplied from melting ice shelves and glaciers (Arrigo et al., 2012). The polynya duration is the length of the open water season. The sea–ice retreat season (when the polynya opens) and advance season (when the polynyas closes) are bound by a positive feedback: early sea–ice retreat in spring/summer implies more solar input at the sea surface since the albedo of seawater is lower than that of sea–ice. More solar input subsequently leads to later and lower sea–ice formation in the advance season

(autumn) (Nihashi and Ohshima, 2001; Stammerjohn et al., 2012). It is worth noting that in 2022, when the in situ data of this study were collected, has been a year of record-breaking low summer Antarctic sea–ice extent (even though this record has then been broken in 2023, Purich and Doddridge, 2023). Turner et al. (2022) and Yadav et al. (2022) identified that a deep ASL in spring associated with the Southern Annular Mode in a positive phase enhanced the sea–ice melting during this anomalously low summer sea–ice year. However the effect of the ASL on the air–sea fluxes is twofold and opposite. On one hand a deeper ASL enhances the southerly flow, pushing the sea–ice away from the shore, widening the polynya and therefore allowing more shortwave radiation to enter the upper ocean leading to a radiative heat gain by the ocean. While on the other hand, we show in our study that the southerly winds bring cold and dry continental air leading to turbulent heat loss. While the main component of the net air–sea heat flux in summer remains the radiative heat flux, we show that synoptic-scale events can set large episodic turbulent fluxes that reduce the net heat flux. Given that the Antarctic sea–ice seems to have reached a new state in recent years (Purich and Doddridge, 2023), it is important to deepen our understanding of the complex atmosphere–ice–sea system. For instance, Stewart et al. (2019) show near the Ross Sea polynya that the ice shelf basal melting from surface heating is more important than what is traditionally thought and is expected to increase in the future. Based on our results, we propose that the dynamics controlling turbulent heat fluxes in these climate sensitive regions should be considered as well.

4.4 Outlook

A number of potential avenues of work became clear during the course of this study. (i) As mentioned earlier, it would be interesting to have THF observations when the ASL is further east, to better understand the dependence of flux variability on the ASL. This corresponds to the austral winter or autumn (Hosking et al., 2016): seasons where we currently lack observations. (ii) The air–sea heat flux is the sum of the turbulent and the radiative components. We hypothesize that the bias in ERA5 THF induced by the land–sea boundary would affect the radiative fluxes as well, with a misrepresentation of the albedo. (iii) Finally, we could expect numerical models with higher spatial resolution than ERA5 to better capture the THF magnitude and variability along the ice shelves. We could therefore compare the observations to some high resolution regional climate models (e.g. MetUM, RACMO) to evaluate their accuracy in a coastal shelf sea such as the Amundsen Sea.

Appendix A: Data processing: investigating the wind distortion effects

The anemometers on a ship can be positioned in a place where they experience airflow distortion from the superstructure of the research vessel (Yelland et al., 1998; Moat et al., 2005; Landwehr et al., 2020). The consequence is a bias in the wind speed values that depends on the location of the anemometers and the shape of the research vessel (Moat et al., 2005). We use ERA5 to analyse the residuals (i.e. research vessel minus ERA5 wind speed) and to validate the in situ wind measurements (Fig. A1).
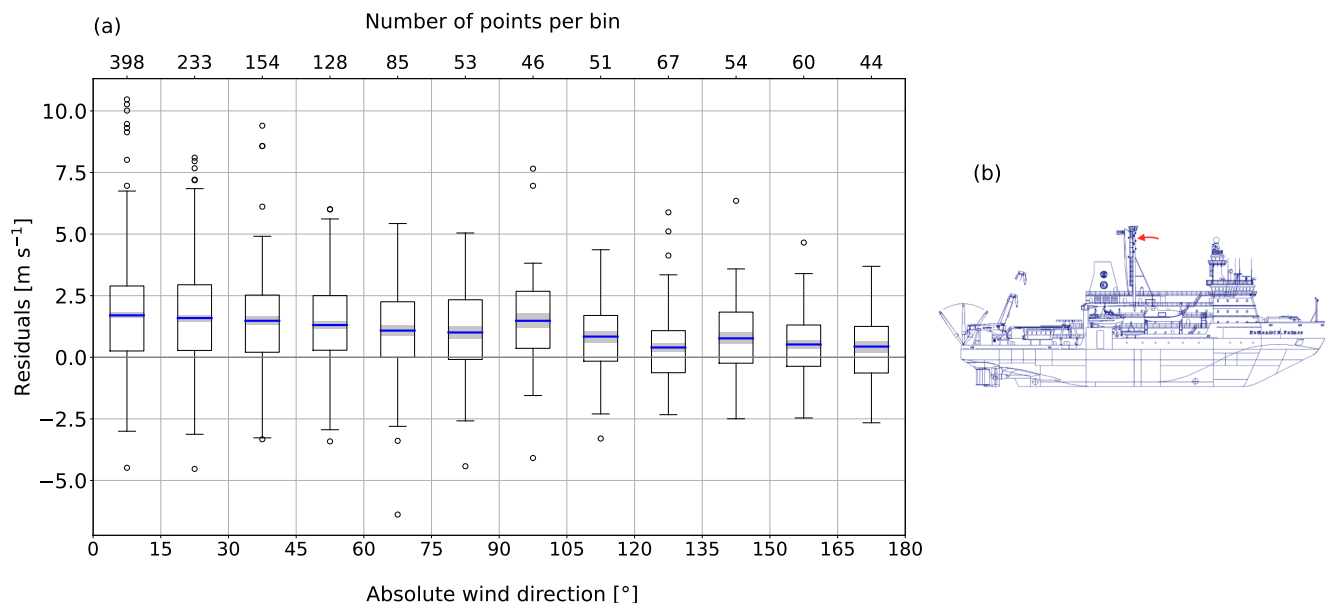
Figure A1. (a): residuals (10-meters wind speed[ship minus ERA5]) binned into 15 degrees relative absolute wind direction. "Relative" means relative to the ship, the convention is the following: a 0° relative wind direction means the wind is blowing bow-on. "Absolute" refers to the assumption that the flow is symmetrically distorted on the port and starboard side: e.g. the wind coming from (75, 90]° and from (-90, -75]° are distorted in the same way and therefore congregated in the same bin. The boxes extend from the lower to the upper quartile values, the whiskers represent the range of the data and the black empty circles are outliers. The outliers are defined as data points lying outside the interval [Q1 - 1.5(Q3-Q1) ; Q3 + 1.5(Q3-Q1)]. The blue lines are the mean per bin. The grey shaded areas indicate the standard error of the mean. (b) is RV *Nathaniel B. Palmer* (adapted from https://www.usap.gov/USAPgov/vesselScienceAndOperations/documents/NBP_Guide.pdf), the red arrow indicates the position of the anemometers.

We observe a decreasing residual with wind blowing from the stern, which could be explained by the openness of the superstructure over the back half of the ship (Fig. A1b). The residuals are positive for each bin, this is possibly an overestimate of the measured wind speed but also a bias from ERA5. We assume the bias is from ERA5 as it has been shown that it is biased low along the Antarctic coast (Caton Harrison et al., 2022). The mean residuals (blue lines, Fig. A1a) are low: the minimum is 0.40 m s^{-1} for the bin (120, 135]° and the maximum is 1.70 m s^{-1} for the bin (0, 15]° (winds blowing from the bow), we therefore decide to keep the data as the bias is not large.

Appendix B: Reynolds decomposition

The Reynolds decomposition consists on the decomposition of a variable X into the sum of its average ($\bar{X}$) and anomaly (X'). We applied this decomposition to the turbulent flux, and hereafter are the mathematical steps that led to the formulation of Equations 6 and 7.

$$\text{SHF} = \rho_{air} C_p (\overline{C_t} + C_t')(\overline{U} + U')(\overline{\Delta T} + \Delta T')$$

$$\text{LHF} = \rho_{air} L_v (\overline{C_q} + C_q')(\overline{U} + U')(\overline{\Delta q} + \Delta q')$$

We expand these equations and average them ($\bar{}$). We use the following averaging rules:

$$\overline{X'} = 0$$

$$\overline{\bar{X}\bar{Y}} = \bar{X}\bar{Y}$$

$$\overline{\bar{X}Y'} = \bar{X}\overline{Y'} = \bar{X} \times 0 = 0$$

We obtain:

$$\overline{\text{SHF}} = \rho_{air} C_p \left[\bar{C_t}\bar{U}\bar{\Delta T} + \bar{C_t}\overline{U'\Delta T'} + \bar{U}\overline{C_t'\Delta T'} + \bar{\Delta T}\overline{U'\Delta C_t'} + \overline{\Delta T'C_t'U'} \right]$$

$$\overline{\text{LHF}} = \rho_{air} L_v \left[\bar{C_q}\bar{U}\bar{\Delta q} + \bar{C_q}\overline{U'\Delta q'} + \bar{U}\overline{C_q'\Delta q'} + \bar{\Delta q}\overline{U'\Delta C_q'} + \overline{\Delta q'C_q'U'} \right]$$

We then subtract the averaged $\overline{\text{SHF}}$ (resp. $\overline{\text{LHF}}$) to the total SHF (LHF) to retrieve the anomalous SHF' (LHF') of Eq. 6 (Eq. 7).
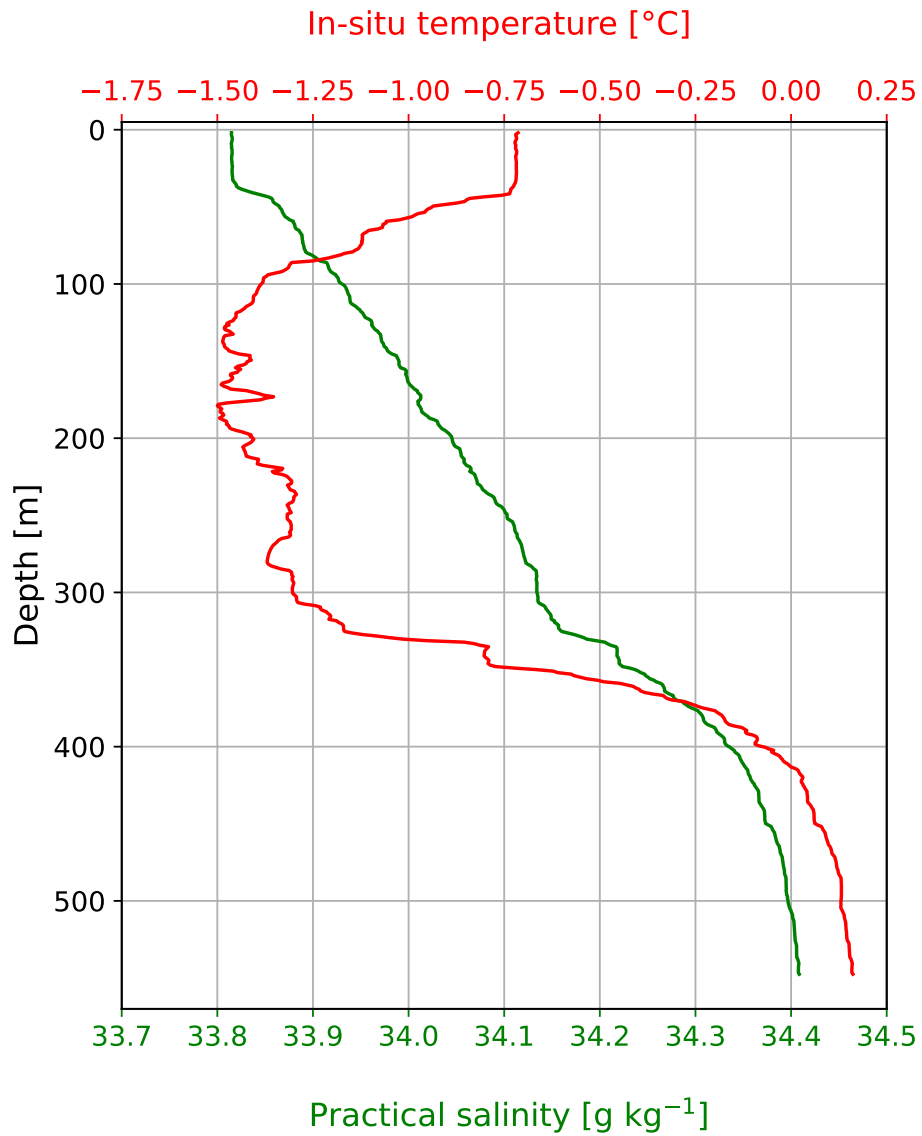
Appendix C: PWP model input

Figure C1. Oceanic forcing: initial temperature and salinity profiles for the PWP simulations from the CTD cast taken at 74.02° S, 113° W.
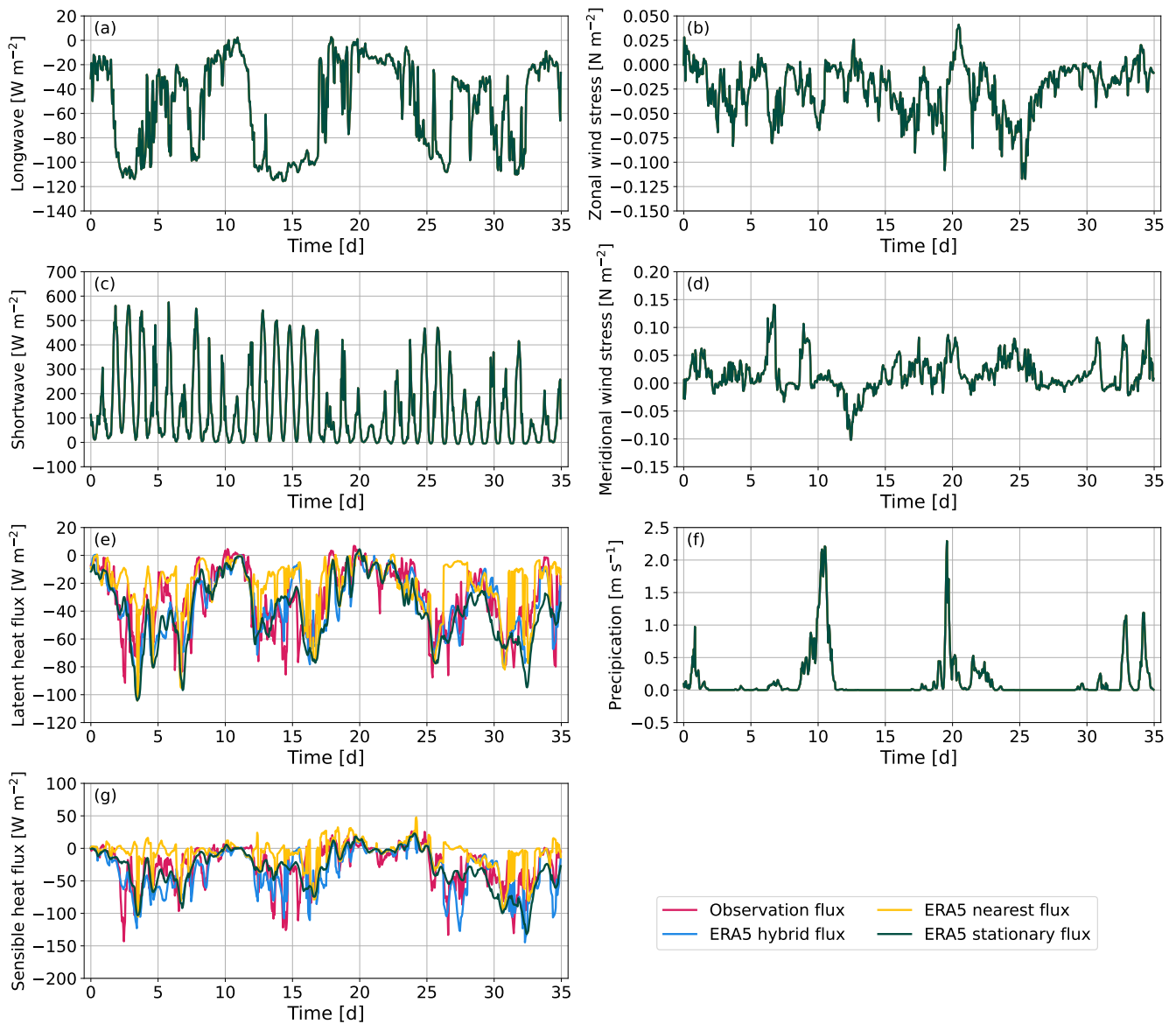
Figure C2. Atmospheric forcing: four runs were performed, only the latent and sensible heat flux differ. The shortwave, longwave and wind stress come from the research vessel observations. The precipitation comes from ERA5 stationary dataset because there was no observation of precipitation from the research vessel.

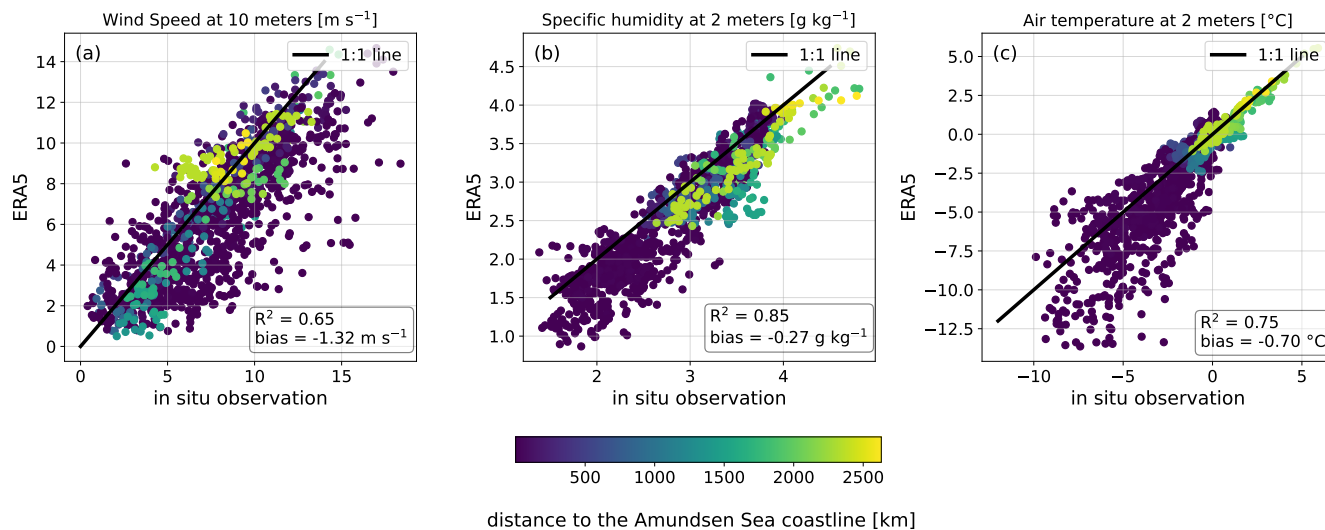# Appendix D: In situ observations and ERA5 sea surface variables comparison

Figure D1. Figure D1: Comparison of (y-axis) ERA5 and (x-axis) in situ observations for (a) wind speed at 10 meters, (b) specific humidity at 2 meters and (c) air temperature at 2 meters. The in situ observations were adjusted down to 10 and 2 meters thanks to AirSeaFluxCode which applies a logarithmic adjustment and stability functions to account for atmospheric stability. To determine specific humidity from ERA5, we convert the dewpoint temperature to specific humidity using the saturation vapour pressure function of Buck (2012). The scatters are colored by the distance to the Amundsen Sea coastline in kilometers, that is defined as the closest coast point in the region lat = [73.66 ; 75.27]°S, lon =[108.10 ; 122.64]°W to the ship position.

460

465

References

Arrigo, K. R. and van Dijken, G. L.: Phytoplankton dynamics within 37 Antarctic coastal polynya systems, Journal of Geophysical Research: Oceans, 108, 2003.

470 Arrigo, K. R., Lowry, K. E., and van Dijken, G. L.: Annual changes in sea ice and phytoplankton in polynyas of the Amundsen Sea, Antarctica, Deep Sea Research Part II: Topical Studies in Oceanography, 71, 5–15, 2012.

Bigg, G. R., Jickells, T. D., Liss, P. S., and Osborn, T. J.: The role of the oceans in climate, International Journal of Climatology: A journal of the Royal Meteorological Society, 23, 1127–1159, 2003.

Biri, S., Cornes, R. C., Berry, D. I., Kent, E. C., and Yelland, M. J.: AirSeaFluxCode: Open-source software for calculating turbulent air-sea

475 fluxes from meteorological parameters, Frontiers in Marine Science, 9, 1049 168, 2023.

Bourassa, M. A., Gille, S. T., Bitz, C., Carlson, D., Cerovecki, I., Clayson, C. A., Cronin, M. F., Drennan, W. M., Fairall, C. W., Hoffman, R. N., et al.: High-latitude ocean and sea ice surface fluxes: Challenges for climate research, Bulletin of the American Meteorological Society, 94, 403–423, 2013.

Bracegirdle, T. J. and Marshall, G. J.: The reliability of Antarctic tropospheric pressure and temperature in the latest global reanalyses,

480 Journal of Climate, 25, 7138–7146, 2012.

Bromwich, D. H., Nicolas, J. P., and Monaghan, A. J.: An assessment of precipitation changes over Antarctica and the Southern Ocean since 1989 in contemporary global reanalyses, Journal of Climate, 24, 4189–4209, 2011.

Buck: Model CR-1A hygrometer with autofill operating manual, Tech. rep., Buck Research Instruments, LLC, 2012.

Caton Harrison, T., Biri, S., Bracegirdle, T. J., King, J. C., Kent, E. C., Vignon, É., and Turner, J.: Reanalysis representation of low-level

485 winds in the Antarctic near-coastal region, Weather and Climate Dynamics, 3, 1415–1437, 2022.

Cayan, D. R.: Variability of latent and sensible heat fluxes estimated using bulk formulae, Atmosphere-Ocean, 30, 1–42, 1992.

Chuda, T., Niino, H., Yoneyama, K., Katsumata, M., Ushiyama, T., and Tsukamoto, O.: A statistical analysis of surface turbulent heat flux enhancements due to precipitating clouds observed in the tropical western Pacific, Journal of the Meteorological Society of Japan. Ser. II, 86, 439–457, 2008.

490 Cronin, M. F., Gentemann, C. L., Edson, J., Ueki, I., Bourassa, M., Brown, S., Clayson, C. A., Fairall, C. W., Farrar, J. T., Gille, S. T., et al.: Air-sea fluxes with a focus on heat and momentum, Frontiers in Marine Science, 6, 430, 2019.

Edson, J. B., Jampana, V., Weller, R. A., Bigorre, S. P., Plueddemann, A. J., Fairall, C. W., Miller, S. D., Mahrt, L., Vickers, D., and Hersbach, H.: On the exchange of momentum over the open ocean, Journal of Physical Oceanography, 43, 1589–1610, 2013.

Fairall, C. W., Bradley, E. F., Rogers, D. P., Edson, J. B., and Young, G. S.: Bulk parameterization of air-sea fluxes for tropical ocean-global

495 atmosphere coupled-ocean atmosphere response experiment, Journal of Geophysical Research: Oceans, 101, 3747–3764, 1996.

Fiedler, E., Lachlan-Cope, T., Renfrew, I., and King, J.: Convective heat transfer over thin ice covered coastal polynyas, Journal of Geophysical Research: Oceans, 115, 2010.

Forster, P., Storelvmo, T., Armour, K., Collins, W., Dufresne, J.-L., Frame, D., Lunt, D., Mauritsen, T., Palmer, M., Watanabe, M., et al.: The Earth's energy budget, climate feedbacks, and climate sensitivity, 2021.

500 Garcia, C., Comiso, J. C., Berkelhammer, M., and Stock, L.: Interrelationships of sea surface salinity, chlorophyll-α concentration, and sea surface temperature near the Antarctic ice edge, Journal of Climate, 34, 6069–6086, 2021.

Hersbach, H., Bell, B., Berrisford, P., Hirahara, S., Horányi, A., Muñoz-Sabater, J., Nicolas, J., Peubey, C., Radu, R., Schepers, D., et al.: The ERA5 global reanalysis, Quarterly Journal of the Royal Meteorological Society, 146, 1999–2049, 2020.

Hosking, J. S., Orr, A., Marshall, G. J., Turner, J., and Phillips, T.: The influence of the Amundsen–Bellingshausen Seas low on the climate of West Antarctica and its representation in coupled climate model simulations, Journal of Climate, 26, 6633–6648, 2013.

Hosking, J. S., Orr, A., Bracegirdle, T. J., and Turner, J.: Future circulation changes off West Antarctica: Sensitivity of the Amundsen Sea Low to projected anthropogenic forcing, Geophysical Research Letters, 43, 367–376, 2016.

Jones, R., Renfrew, I., Orr, A., Webber, B., Holland, D., and Lazzara, M.: Evaluation of four global reanalysis products using in situ observations in the Amundsen Sea Embayment, Antarctica, Journal of Geophysical Research: Atmospheres, 121, 6240–6257, 2016.

Jones, R. W.: Weather and climate in the Amundsen Sea Embayment, West Antarctica: observations, reanalyses and high resolution modelling, Ph.D. thesis, University of East Anglia, 2018.

Kim, C.-S., Kim, T.-W., Cho, K.-H., Ha, H. K., Lee, S., Kim, H.-C., and Lee, J.-H.: Variability of the Antarctic Coastal Current in the Amundsen Sea, Estuar. Coast. Shelf S., 181, 123–133, https://doi.org/10.1016/j.ecss.2016.08.004, 2016.

Kumar, A., Yadav, J., and Mohan, R.: Seasonal sea-ice variability and its trend in the Weddell Sea sector of West Antarctica, Environmental Research Letters, 16, 024 046, 2021.

Landwehr, S., Thurnherr, I., Cassar, N., Gysel-Beer, M., and Schmale, J.: Using global reanalysis data to quantify and correct airflow distortion bias in shipborne wind speed measurements, Atmospheric Measurement Techniques, 13, 3487–3506, 2020.

Moat, B., Yelland, M., and Molland, A.: The effect of ship shape and anemometer location on wind speed measurements obtained from ships, 2005.

Morales Maqueda, M. A., Willmott, A. J., and Biggs, N.: Polynya dynamics: A review of observations and modeling, Reviews of Geophysics, 42, 2004.

Morlighem, M., Rignot, E., Binder, T., Blankenship, D., Drews, R., Eagles, G., Eisen, O., Ferraccioli, F., Forsberg, R., Fretwell, P., et al.: Deep glacial troughs and stabilizing ridges unveiled beneath the margins of the Antarctic ice sheet, Nature geoscience, 13, 132–137, 2020.

Nihashi, S. and Ohshima, K. I.: Relationship between the sea ice cover in the retreat and advance seasons in the Antarctic Ocean, Geophysical research letters, 28, 3677–3680, 2001.

Ogle, S., Tamsitt, V., Josey, S., Gille, S., Cerovečki, I., Talley, L., and Weller, R.: Episodic Southern Ocean heat loss and its mixed layer impacts revealed by the farthest south multiyear surface flux mooring, Geophysical Research Letters, 45, 5002–5010, 2018.

Ohshima, K. I., Yoshida, K., Shimoda, H., Wakatsuchi, M., Endoh, T., and Fakuchi, M.: Relationship between the upper ocean and sea ice during the Antarctic melting season, Journal of Geophysical Research: Oceans, 103, 7601–7615, 1998.

Papritz, L., Pfahl, S., Sodemann, H., and Wernli, H.: A climatology of cold air outbreaks and their impact on air–sea heat fluxes in the high-latitude South Pacific, Journal of Climate, 28, 342–364, 2015.

Price, J. F., Weller, R. A., and Pinkel, R.: Diurnal cycling: Observations and models of the upper ocean response to diurnal heating, cooling, and wind mixing, Journal of Geophysical Research: Oceans, 91, 8411–8427, 1986.

Purich, A. and Doddridge, E. W.: Record low Antarctic sea ice coverage indicates a new sea ice state, Communications Earth & Environment, 4, 314, 2023.

Queste, B., Jacob, B., and du Plessis, M.: Data used in the manuscript entitled "Turbulent heat flux dynamics along the Dotson and Getz ice-shelf fronts (Amundsen Sea, Antarctica)", Zenodo. https://doi.org/10.5281/zenodo.12647855, 2024.

Renfrew, I. A., King, J. C., and Markus, T.: Coastal polynyas in the southern Weddell Sea: Variability of the surface energy budget, Journal of Geophysical Research: Oceans, 107, 16–1, 2002.

540   Scambos, T. A., Bell, R. E., Alley, R. B., Anandakrishnan, S., Bromwich, D., Brunt, K., Christianson, K., Creyts, T., Das, S., DeConto, R., et al.: How much, how fast?: A science review and outlook for research on the instability of Antarctica's Thwaites Glacier in the 21st century, Global and Planetary Change, 153, 16–34, 2017.

Schaffer, J., Timmermann, R., Arndt, J. E., Kristensen, S. S., Mayer, C., Morlighem, M., and Steinhage, D.: A global, high-resolution data set of ice sheet topography, cavity geometry, and ocean bathymetry, Earth System Science Data, 8, 543–557, 2016.

545   Smith Jr, W. O. and Barber, D.: Polynyas: Windows to the world, Elsevier, 2007.

Spreen, G., Kaleschke, L., and Heygster, G.: Sea ice remote sensing using AMSR-E 89-GHz channels, Journal of Geophysical Research: Oceans, 113, 2008.

Stammerjohn, S., Massom, R., Rind, D., and Martinson, D.: Regions of rapid sea ice change: An inter-hemispheric seasonal comparison, Geophysical Research Letters, 39, 2012.

550   Stewart, C. L., Christoffersen, P., Nicholls, K. W., Williams, M. J., and Dowdeswell, J. A.: Basal melting of Ross Ice Shelf from solar heat absorption in an ice-front polynya, Nature Geoscience, 12, 435–440, 2019.

Swart, S., Gille, S. T., Delille, B., Josey, S., Mazloff, M., Newman, L., Thompson, A. F., Thomson, J., Ward, B., Du Plessis, M. D., et al.: Constraining Southern Ocean air-sea-ice fluxes through enhanced observations, Frontiers in Marine Science, 6, 421, 2019.

Tanimoto, Y., Nakamura, H., Kagimoto, T., and Yamane, S.: An active role of extratropical sea surface temperature anomalies in determining
555   anomalous turbulent heat flux, Journal of Geophysical Research: Oceans, 108, 2003.

Turner, J., Orr, A., Gudmundsson, G. H., Jenkins, A., Bingham, R. G., Hillenbrand, C.-D., and Bracegirdle, T. J.: Atmosphere-ocean-ice interactions in the Amundsen Sea embayment, West Antarctica, Reviews of Geophysics, 55, 235–276, 2017.

Turner, J., Holmes, C., Caton Harrison, T., Phillips, T., Jena, B., Reeves-Francois, T., Fogt, R., Thomas, E. R., and Bajish, C.: Record low Antarctic sea ice cover in February 2022, Geophysical Research Letters, 49, e2022GL098 904, 2022.

560   Yadav, J., Kumar, A., and Mohan, R.: Atmospheric precursors to the Antarctic sea ice record low in February 2022, Environmental Research Communications, 4, 121 005, 2022.

Yang, H., Liu, J., Lohmann, G., Shi, X., Hu, Y., and Chen, X.: Ocean-atmosphere dynamics changes associated with prominent ocean surface turbulent heat fluxes trends during 1958–2013, Ocean Dynamics, 66, 353–365, 2016.

Yelland, M., Moat, B., Taylor, P., Pascal, R., Hutchings, J., and Cornell, V.: Wind stress measurements from the open ocean corrected for
565   airflow distortion by the ship, Journal of physical Oceanography, 28, 1511–1526, 1998.

Yu, L.: Global air–sea fluxes of heat, fresh water, and momentum: Energy budget closure and unanswered questions, Annual review of marine science, 11, 227–248, 2019.

Yu, L.-S., He, H., Leng, H., Liu, H., and Lin, P.: Interannual variation of summer sea surface temperature in the Amundsen Sea, Antarctica, Frontiers in Marine Science, 10, 1050 955, 2023.

570   Zhou, L., Heuzé, C., and Mohrmann, M.: Early winter triggering of the Maud Rise polynya, Geophysical Research Letters, 49, e2021GL096 246, 2022.